Clemson University TigerPrints

All Dissertations Dissertations

8-2011

Low-Resolution Vision for Autonomous Mobile Robots

Vidya Nariyambut murali Clemson University, nmvidya@gmail.com

Follow this and additional works at: https://tigerprints.clemson.edu/all_dissertations



Part of the <u>Electrical and Computer Engineering Commons</u>

Recommended Citation

Nariyambut murali, Vidya, "Low-Resolution Vision for Autonomous Mobile Robots" (2011). All Dissertations. 771. https://tigerprints.clemson.edu/all_dissertations/771

This Dissertation is brought to you for free and open access by the Dissertations at TigerPrints. It has been accepted for inclusion in All Dissertations by an authorized administrator of TigerPrints. For more information, please contact kokeefe@clemson.edu.

Low-Resolution Vision for Autonomous Mobile Robots

A Dissertation
Presented to
the Graduate School of
Clemson University

In Partial Fulfillment
of the Requirements for the Degree
Doctor of Philosophy
Electrical Engineering

by Vidya N. Murali August 2011

Accepted by:

Dr. Stanley T. Birchfield, Committee Chair

Dr. Adam W. Hoover

Dr. Ian D. Walker

Dr. Keith E. Green

Abstract

The goal of this research is to develop algorithms using low-resolution images to perceive and understand a typical indoor environment and thereby enable a mobile robot to autonomously navigate such an environment. We present techniques for three problems: autonomous exploration, corridor classification, and minimalistic geometric representation of an indoor environment for navigation. First, we present a technique for mobile robot exploration in unknown indoor environments using only a single forward-facing camera. Rather than processing all the data, the method intermittently examines only small 32×24 downsampled grayscale images. We show that for the task of indoor exploration the visual information is highly redundant, allowing successful navigation even using only a small fraction (0.02%) of the available data. The method keeps the robot centered in the corridor by estimating two state parameters: the orientation within the corridor and the distance to the end of the corridor. The orientation is determined by combining the results of five complementary measures, while the estimated distance to the end combines the results of three complementary measures. These measures, which are predominantly informationtheoretic, are analyzed independently, and the combined system is tested in several unknown corridor buildings exhibiting a wide variety of appearances, showing the sufficiency of low-resolution visual information for mobile robot exploration. Because the algorithm discards such a large percentage (99.98%) of the information both spatially and temporally, processing occurs at an average of 1000 frames per second, or equivalently takes a small fraction of the CPU.

Second, we present an algorithm using image entropy to detect and classify corridor junctions from low resolution images. Because entropy can be used to perceive depth, it can be used to detect an open corridor in a set of images recorded by turning a robot at a junction by 360 degrees. Our algorithm involves detecting peaks from continuously measured entropy values and determining the angular distance between the detected peaks to determine the type of junction that was recorded (either middle, L-junction, T-junction, dead-end, or cross junction). We show that the same algorithm can be used to detect open corridors from both monocular as well as omnidirectional images.

Third, we propose a minimalistic corridor representation consisting of the orientation line (center) and the wall-floor boundaries (lateral limit). The representation is extracted from low-resolution images using a novel combination of information theoretic measures and gradient cues. Our study investigates the impact of image resolution upon the accuracy of extracting such a geometry, showing that centerline and wall-floor boundaries can be estimated with reasonable accuracy even in texture-poor environments with low-resolution images. In a database of 7 unique corridor sequences for orientation measurements, less than 2% additional error was observed as the resolution of the image decreased by 99.9%.

Dedication

This work is dedicated to all the researchers and scientists who have inspired me all my life to ask questions and be persistent.

Acknowledgments

The first thanks must go to my adviser Dr Stan Birchfield, who has been a wall of support throughout. His patience and foresight have incessantly steered me in the right direction while saving me from numerous pitfalls. He has taught us equanimity, fortitude, perseverance and his teachings will be a positive influence in my life for ever. I must thank Dr Adam Hoover and Dr Ian Walker for teaching me all the important things early on and Dr Keith Green for introducing me to the creative side of robotics in architecture. I also thank them for being on the committee and for their help in directing the research to a credible conclusion by their continuous positive guidance.

I sincerely thank Dr Rick Tyrrell from the Department of Psychology for the research discussions with Dr Stan Birchfield, that introduced us to the influential work by H.W. Leibowitz, that forms the motivation for our work on low-resolution vision.

I thank Dr Andrew Duchowski of the Computer Science department for giving me an opportunity to work in the exciting field of eye-tracking and for granting us permission to use the Tobii eye-tracking equipment.

My fellow research group mates and seniors Zhichao Chen, Neeraj Kanhere, Shrinivas Pundlik and Guang Zeng, have been very kind to me throughout and have helped me in various ways to accomplish my research goals. I particularly thank fellow lab-mates Bryan Willimon and Yinxiao Li for all the research collaborations and the fun discussions we had on robotics and vision. I also thank Anthony Threatt and Joe Manganelli of the Architecture department for teaching me many things during our collaborative efforts for Architectural Robotics class.

Thanks to all the people who helped develop *Blepo* — the computer vision library in our department. It made all the code possible.

I extend my gratitude to all the researchers and students of robotics and vision whose work has influenced and inspired me to start on this venture, without whom this work would not have been possible.

I must extend my gratitude to National Institute of Medical Informatics for their generous Ph.D Fellowship and to the Department of Electrical and Computer Engineering at Clemson for their graduate assistantships throughout my degree program.

I thank Lane Swanson and Elizabeth Gibisch for handling all my graduate paperwork, keeping track of my student status and my assistantships with inimitable patience.

I thank my friends Shubhada, Divina, Salil, Trupti, Ninad, Sumod and Rahul for being there with me through these years. I had a wonderful time at Clemson, mainly due to their unwavering support and friendship.

I thank the elders in the family for being supportive of my decisions and for their blessings and for being there for me at all times. I also thank the young ones for bringing cheer and laughter into my life.

Most of all, I thank my wonderful husband Ashwin, for giving me love and encouragement when I needed it and for being a wall of support in my life.

Table of Contents

Ti	tle F	${ m Page}$	i
A۱	ostra	ct	ii
A۱	ostra	ct	ii
De	edica	tion	V
A	ckno	wledgments	v
Li	st of	Tables i	X
Li	st of	Figures	X
1	Intr 1.1 1.2 1.3 1.4 1.5	Low resolution vision	1 3 5 6 9
2	Pre 2.1 2.2		2
3	Esti 3.1 3.2 3.3 3.4 3.5	Symmetry by mutual information	21 24 25 26 28
4	Esti 4.1 4.2		30 30

	4.3	Entropy	32
5	Filt : 5.1	Noise model development	33
	5.2 5.3	1	42 45
6	Cor	ridor Junction Classification	50
	6.1 6.2	0	50 54
7	Esti	mating Corridor Geometry for Navigation	58
	7.1	Minimalistic corridor geometry	58
	7.2	e v	62
8	Exp	$f erimental\ Results \ldots \ldots \qquad f erimental\ Results \ldots \qquad f erimental\ Results \ldots \qquad f erimental\ Results \qquad f erimental\ Result$	36
	8.1		66
	8.2	S C C C C C C C C C C C C C C C C C C C	68
	8.3		72
	8.4	<u>-</u>	75
	8.5		77
	8.6		79
9	Con	clusion	38
	9.1		39
	9.2		91
Aı	ppen	dices	93
\mathbf{A}	Tim	e-to-contact Relative to a Planar Surface)4
В	Kal	man Filter	9
	B.1	Kalman filter, matrix notation	00
	B.2	Kalman filter in operation)2
\mathbf{C}	Visi	nal Detection of Light Sources	04
Bi	bliog	raphy	በብ

List of Tables

5.1	Parameter values for the Kalman filter	46
8.1	Performance: Time taken by the different vision modules	77
8.2	ROC from confusion matrix	78
8.3	Confusion matrix for corridor classification	79

List of Figures

1.1 1.2 1.3 1.4 1.5	A typical corridor image at seven different resolutions
2.1	A taxonomy of approaches to vision-based navigation
3.1 3.2 3.3 3.4 3.5	Column in image with maximum entropy
5.1 5.2 5.3 5.4 5.5 5.6 5.7 5.8	Noise model for median of ceiling lights3Noise model for maximum entropy3Noise model for maximum symmetry3Noise model for vanishing point3Noise model for aggregate phase4Noise model for distance to end parameters4Orientation estimation using the Kalman filter4Distance to the end estimation using the Kalman filter4
6.1 6.2 6.3 6.4 6.5	Corridor junctions using entropy
7.1 7.2 7.3 7.4	Ullman local contrast criterion
8.1	Buildings for orientation test data

8.2	Estimating the center of the corridor using various cues	69
8.3	Sample images from the orientation estimation in one corridor	70
8.4	Orientation estimation from 5 measures	70
8.5	Distance to end estimate from 3 measures	71
8.6	Exploration experiments for ten different corridors	74
8.7	Problematic Corridors	75
8.8	Rapid perception for three different corridors	76
8.9	ROC curve for corridor classification	79
8.10	Mean error for orientation estimation	81
8.11	Comparison of results with Kong et al	82
8.12	Additional results for other corridors	83
8.13	Corridor structure reconstruction from the wall-floor boundary	85
8.14	Mean error for lateral position and width estimation	86
8.15	minimalistic representation in 4 resolutions	87
A.1	Perspective projection	95
	Camera motion	

Chapter 1

Introduction

1.1 Low resolution vision

It has been known for some time that natural visual systems contain parallel pathways for recognition and guidance [100, 94, 77]. While recognition capabilities deteriorate severely under poor visual conditions such as low-resolution or low illumination, guidance capabilities remain largely intact. Studying the behavior of human drivers under adverse conditions, Leibowitz et al. [48, 69, 11] proposed the "selective degradation hypothesis" to explain the fact that some visual abilities such as vehicle steering and speed control remain relatively easy despite significant loss in visual acuity and color vision. Their psychovisual experiments revealed that the subjective magnitude of vection (that is, the vivid sensation of self-motion induced by optical flow in the visual field) is unaffected by reductions of luminance of eight orders of magnitude and by refractive errors of up to 20 diopters. In contrast, virtually all aspects of focal vision (e.g., visual acuity, peak contrast sensitivity, and accommodation) deteriorate rapidly when light levels drop from daytime to night. Therefore, it seems plausible that artificial robotic systems should be capable of solving guidance

tasks such as exploration and navigation even with impoverished sensing.

In related research, Schneider [2] showed that animals with poor vision were able to orient themselves toward salient visual events. This research not only confirms the use of low resolution sensor data but also highlights a specific application, namely, detecting salient regions in the visual field. Similarly, we envision mobile robotic systems that automatically orient themselves toward visually salient regions (or locations) using low-resolution images. For example, a mobile robot could measure the image entropy (as an information theoretic measure of saliency) in order to orient itself toward an open corridor (the salient region).

Furthermore, psychological studies have shown that a human's gaze while driving or walking is determined largely by minimalistic information from the environment. More specifically, people tend to focus their eye gaze on the direction of the goal and also along bend points (tangent points) in curved roadways [102, 47]. Therefore, in indoor corridor environments we expect a minimalistic representation (consisting of vanishing points and wall-floor boundaries) to be sufficient for mobile robot navigation.

There has also been psychological and artistic perception of low-resolution vision, in which low-resolution movies are produced using very few LEDs (pixelated representation).¹ Even though the individual objects are not discernible at that resolution, the human visual system is able to fill in gaps in the abstract data [24], making the moving image perceivable. Such work validates the concept of low-resolution imagery.

¹http://www.jimcampbell.tv/portfolio/low_resolution_works/

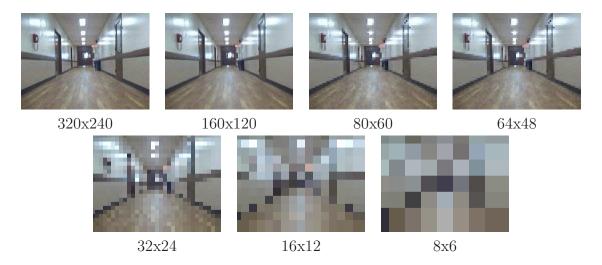


Figure 1.1: A typical corridor image at seven different resolutions. Even in resolutions as low as 32×24 , it is easy to recognize the structure of the corridor. For display purposes, the downsampled images we resized so that all of the images are shown in the same size.

1.2 The three problems

Motivated by these psychological studies, we present solutions to three problems. First we present an algorithm for estimating the robot's orientation in the corridor along with its distance to the end of the corridor to enable autonomous exploration in a typical unknown indoor environment. Our solution combines a number of complementary information theoretic measures obtained from low-resolution grayscale images. After describing these individual measures, we present an integrated system that is able to autonomously explore an unknown indoor environment, recovering from difficult situations like corners, blank walls, and initial heading toward a wall. All of this behavior is accomplished at a rate of 1000 Hz on a standard computer using only 0.02% of the information available from a standard color VGA (640×480) video camera, discarding 99.98% of the information.

Second, we present a simple peak detection algorithm using a mixture of Gaussians to detect and classify corridor junctions from forward facing monocular as well

as omnidirectional images. We show that entropy alone as a measure is enough to detect open corridors even at a resolution as low as 32×24 . We present an analysis of the relationship between image entropy and depth of a corridor in an indoor environment. The spatial property of entropy can be used to give a description of corridor depth that has direct applications in autonomous corridor navigation using monocular vision.

Third, we propose a minimalistic representation of a corridor using three lines that capture the center of the corridor, the left wall-floor boundary, and the right wall-floor boundary — the intersection of the orientation (center) line with the wall-floor boundary detected is the vanishing point. We combine ceiling lights with other metrics such as maximum entropy and maximum symmetry to estimate the center of the corridor when ceiling lights are not visible. We also introduce the use of a measure of local contrast in pixels as explained by Ullman [95] for reducing the effect of specular reflections off the floor and walls. In our experiments, we present data to establish the best resolution for a mobile robot to explore an indoor corridor, considering the accuracy and time efficiency. Although higher resolutions may provide richer information like door frames and sign recognition, which can be used for scene interpretation, they are not necessary for basic robot navigation tasks.

For all three problems, we use low-resolution 32×24 grayscale images. For all results, we simply downsample the image without smoothing, which decreases computation time significantly by avoiding touching every pixel. Although there are good theoretical reasons to smooth before downsampling, we adopt this extreme approach to test the limits of such an idea. From the example in Figure 1.1, it can be seen that the discernible elements of a corridor that enable recognition remain fairly consistent across resolutions until 32×24 .

Why study low resolution? First, the reduced amount of data available leads to

greatly reduced processing times, which can be used either to facilitate the use of low-cost, low-power embedded processors, or to free up the processor to spend more cycles on higher-level focal vision tasks such as recognition. Secondly, the impoverished sensor necessarily limits the variety of algorithms that can be applied, thus providing focus and faster convergence to the research endeavor. Finally, by restricting ourselves to such impoverished sensory data, it is possible to make quantitative claims about how much information is needed to accomplish a given task.

1.3 Monocular vision as the sensor

Vision is potentially more informative than other sensors because vision provides different kinds of information about the environment, while other sensors (such as sonars or lasers) only provide depth. For landmark detection and recognition, vision provides direct ways to do so and is easy to represent because of the close relation to the way humans understand landmarks. In addition lasers are expensive and power-hungry, and sonars cause interference.

Navigating with a single camera is not easy. Perhaps this is why many approaches rely upon depth measurements from sonars, lasers, or stereo cameras to solve the problem. Granted, knowledge of distances to either wall, the shape of obstacles, and so on, would be directly useful for localizing the robot and building a geometric map of the environment. Stereo vision has its own difficulties (e.g., it requires texture to compute correspondence, is computationally expensive and produces inaccurate results for many pixels). Indoor environments in particular often lack texture, rendering stereo matching an elusive problem in such places. In contrast, humans are quite good at navigating indoors with one eye closed, even with blurry vision, thus motivating us to find a different solution.

1.4 What resolution is needed?

1.4.1 Information content in an image

To get a sense of the visible content in a typical corridor image, Fig. 1.2 shows an example image at successively downsampled resolutions. It can be seen that as the image is decreased in size from 640×480 to 32×24 , the corridor remains recognizable. However, at the resolution of 16×12 , a noticeable drop in recognizability occurs, in which it is difficult to discern that the image is of a corridor at all. This observation is confirmed by noting that the Fourier coefficients are dominated by the low-frequency terms.

To quantify these results, let $I: \Omega \to \mathcal{V}$ be a grayscale image, where $\mathbf{x} = (x,y) \in \Omega \subset \mathbb{R}^2$ are the coordinates of a pixel in the image plane, $v \in \mathcal{V} = \{0,\ldots,2^n-1\}$ is a scalar intensity value, and n is the number of bits per pixel. If we assume that the pixel values in the image were drawn independently according to the probability mass function (PMF) p(v), then we can say that

$$H(V; I) = \sum_{v \in \mathcal{V}} -p(v)\log p(v), \tag{1.1}$$

is a measure of the information content in the image, where H(V; I) is the entropy¹ of a random variable V with PMF p(v). Typically p(v) is estimated by the normalized graylevel histogram of the image. The entropy of an image is a scalar representing the statistical measure of randomness that can be used to characterize its texture. According to Shannon's theory of entropy [82], the entropy is the measure of information content of a random variable and the rarer the random variable's occurrence

¹Note that by the term *entropy*, we mean the quantity defined according to information theory. Other definitions of entropy, such as those used in thermodynamics or other fields, are not relevant to this work.

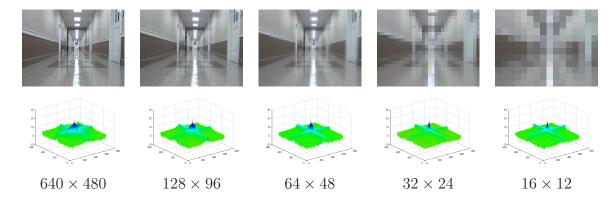


Figure 1.2: Top: A typical corridor shown at different image resolutions. As the image resolution drops from 640×480 to 32×24 , the pattern of the corridor is still observable, but at 16×12 it is difficult to recognize the scene at all. Bottom: The corresponding Fourier coefficients (logarithmic display) show that the low frequency coefficients are more prominent.

the greater the information content of the random variable. Fig. 1.3 shows that for a variety of environments, the entropy of an image does not change significantly as the image is downsized from 640×480 to 32×24 . In fact, at the latter resolution, there is only a 5% drop in entropy from the original image. However, as the resolution drops below 32×24 , the entropy drops sharply.

Of course, the entropy of the random variable associated with the graylevel values of the pixels in an image is not the only way to measure information content. As a result, this experiment does not necessarily establish any validity to the claim that for any given task such a resolution is sufficient. However, we argue that there is a close connection between the coarse information needed for autonomous guidance (whether exploration or navigation) of a mobile robot and the more general problem of scene recognition. In both cases, the task is aimed at gleaning summary information from the entire image rather than discovering particular identities of objects in the scene. To this end, it is interesting to note that our results are similar to those of Torralba and colleagues [90, 91]. Their independent work on determining the spatial resolution limit for scene recognition has established through psychovisual

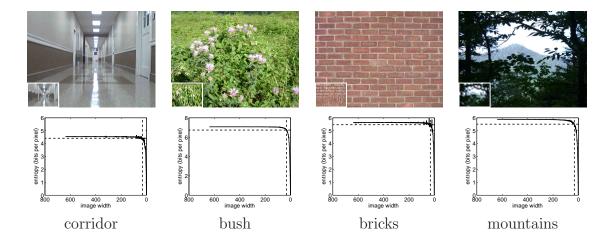


Figure 1.3: Plots of entropy versus image resolution for four different scene types. A loss of just 5% of information occurs as the image is downsized from 640×480 to 32×24 , but a sharp drop follows even lower resolutions. For each image, the inset in the lower-left corner shows the 32×24 version (upsampled for display) in which the scene is clearly recognizable.

experiments that 32×32 is sufficient for the identification of semantic categories of real world scenes. Our result of 32×24 is a close approximation governed by the desire to preserve the aspect ratio of the original image. As we shall see, these resolutions are corroborated by our own experiments on the specific task of autonomous exploration of a mobile robot.

1.4.2 Discernible segments in an image

A scene is often interpreted by the individual objects in it. Often objects are discernible even when the resolution is poor. Torralba et~al.~[91, 90] have shown that successful object segmentation and identification can be achieved by humans observing 32×32 color images. We see that simple computer vision based segmentation techniques show the same interesting result. The effect of k-means segmentation in an image as the resolution drops is stable. That is, the mean values remain relatively constant as the size of the image drops from 640×480 to 32×24 . Furthermore,

the segments are discernible and distinct even as resolution drops and they begin to coalesce only after the resolution of 32×24 . See Figures 1.4 and 1.5.

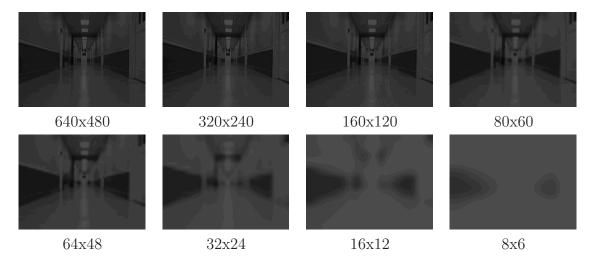


Figure 1.4: The figure shows the k-means segmentation results on a typical corridor image with k=10. It can be seen that the individual segments are discernible and consistent across resolutions until the resolution of 32×24 . For resolutions lower than that, the segments begin to merge.

From the above discussions, we can see that there is sufficient evidence from a number of sources: psychology, independent research by Torralba $et\ al.$ [90, 91], information theoretic measurements on images (entropy) and observing the segmentation of images across resolutions, that 32×24 seems to be approximately the optimal low-resolution that is necessary and sufficient for a variety of simple tasks like detection and recognition. We will show that the same confidence can be extended to robot navigation/exploration tasks.

1.5 Outline of this dissertation

The next chapter gives a summary of the work done previously in vision based navigation, the different approaches, the achievements, limitations, and ongoing work. Chapters 3, 4, 5, and 6 describe the detailed structure of the algorithms, the percepts,

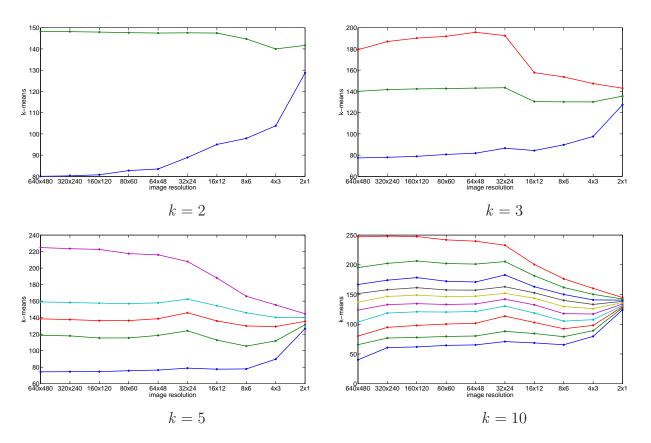


Figure 1.5: The variation of the mean values for different values of k. It can be seen that when resolution drops, the mean values do not change significantly until 32×24 after which all means converge rapidly. This highlights that objects in an image retain their composition in general as resolution drops until the approximately optimal size of 32×24 .

the visual processing for navigation. Chapter 7 discusses a number of experiments conducted on the robot in an indoor environment, with supporting plots, graphs and image sequences. These give us a sense of the reliability of the algorithms and their limitations. Chapter 8 gives a summary of the dissertation, an outline of future work and concluding discussions.

Chapter 2

Previous Work

2.1 Low-resolution vision

Experiments conducted by Torralba and Sinha [92] have established lower bounds on image resolution needed for reliable discrimination between face and non-face patterns, indicating that the human visual system is surprisingly effective at detecting faces in low resolutions. Similarly, Hayashi and Hasegawa [26] have developed a method that achieves a face detection rate of 71% for as small as 6×6 face patterns extracted from larger images. Torralba $et\ al.\ [91,\ 90]$ in their recent work have presented several psychovisual experiments to show that 32×24 images are sufficient for human beings to successfully performs basic scene classification, object segmentation, identification . They have shown results on an extensively constructed database of 80 million images that make a powerful argument in favor of low-resolution vision for non-parametric object and scene recognition. The application to person detection and localization is particularly noteworthy considering that they have produced good results with low-resolution images that are comparable to that of the Viola-Jones detector which uses high-resolution images. The whole spirit

of low-resolution is strengthened by this argument and one can see that low-resolution images provide enough information for basic visual processing. Judd $et\ al.$ [34] conducted psycho-visual experiments to investigate how image resolution affects fixation locations and consistency across humans through an eye-tracking experiment. They found that fixations from lower resolution images can predict fixations on higher resolution images, that human fixations are biased toward the center for all resolutions, and this bias is stronger at lower resolutions. Furthermore they found that human fixations become more consistent as resolution increases until around 16-64 pixels (1/2 to 2 cycles per degree) after which consistency remains relatively constant despite the spread of fixations away from the center. Here again the work shows interestingly consistent results at image resolutions 32×32 .

There is a connection between low-resolution vision and the notion of scale space [103, 50]. Scale space processing emphasizes extracting information from multiple scales and is the basis of popular feature detection algorithms such as SIFT [52] and SURF [5]. Koenderink [40] speaks of the "deep structure" within images, arguing that human visual system perceives images at several levels of resolution simultaneously. His distinction between deep and superficial structure is closely related to the distinction between focal (for recognition) and ambient (for guidance) vision [100].

There is also a recent emphasis on minimalistic sensing. Tovar et al. [93] in their recent work have developed an advanced data structure for constructing a minimal representation based entirely on critical events in online sensor measurements made by the robot. The goal was to enable mobile robotic systems to perform sophisticated visibility-based tasks with minimal sensing requirements. Because previous algorithmic efforts like SLAM often assume the availability of perfect geometric models, they are susceptible to problems such as mapping uncertainty, registration, segmentation, localization and control errors. In their work, depth discontinuities

are encoded in a simple data structure called the Gap Navigation Tree (GNT) which evolves over time from online sensor measurements (two laser range sensors), to provide the robot the shortest path to the goal. O'Kane and LaValle in their work [68] have described an 'almost-sensorless localization' system, using only a compass, a contact sensor and a map of the environment. Because no odometry is available, the robot can only make make maximal linear motions in a chosen direction in an environment till the limits. The history of such actions is also available to the robot. They have shown that a simple system like this is actually capable of localization.

There has also been an emphasis on 'lightweight' or 'low-feature' SLAM techniques with the goal of reducing the computational burden in embedded robotic systems. Nguyen et al. [67] have developed a system that performs lightweight SLAM, an algorithm that uses only perpendicular or parallel lines in the environment for mapping because they represent the main structure of most of the indoor environments. By using orthogonality as a geometric constraint in the environment, many unwanted dynamic objects are removed in the desired reconstruction leading to a rather precise and consistent mapping. This is synonymous with the spirit of downsampling an image to remove noise/reflections. Choi et al. [16] have also developed a line-feature based SLAM in a geometrically constrained extended Kalman filter framework. They have developed an efficient line extraction algorithm that works on measurements obtained from sparse, low-grade sensors which reduce the search space by representing the indoor environment using a combination of these line features. They have shown results in which a room has been modeled using the geometry of the room as well as rectangular objects present in the room. Localization is shown to be achieved with good accuracy even with impoverished sensor information.

Representation of indoor environments has largely been geometric. While previous studies suggest that humans rely on geometric visual information (hallway

structure) rather than non-geometric visual information (e.g., doors, signs and lighting) for acquiring cognitive maps of novel indoor layouts, Kalia *et al.* [35] in their recent work have shown that humans rely on both geometric and non-geometric cues under constraints of low-vision.

Vision-based mobile robot navigation has been studied by many researchers. From the early work of the Stanford Cart [63] to the current Aibo (the toy robot built by Sony), navigation has been recognized as a fundamental capability that needs to be developed. According to the survey of DeSouza et al. [22], significant achievements have been made in indoor navigation, with FINALE [45] being one of the more successful systems. FINALE requires a model-based geometric representation of the environment and uses ultrasonic sensors for obstacle avoidance. NEURO-NAV [59] is another oft cited system that uses a topological representation of the environment and responds to human-like commands. RHINO [12] is an example of a robust indoor navigating robot. The highly notable NAVLAB [88] is an example of proficient outdoor navigation system which use a combination of vision and a variety of other sensors for navigation and obstacle avoidance. Moravec [63] and Nelson et al. [66], however, have emphasized the importance of low-level vision in mobile robot navigation, and Horswill [30] implemented a hierarchical and complete end-to-end vision-based navigational robot based on prior training of the environment.

Historically, low-resolution images have been used for various mobile robotic tasks because of the limitations of processing speeds. For example, in developing a tour-giving autonomous navigating robot, Horswill [31] used 64×48 images for navigation and 16×12 images for place recognition. Similarly, the ALVINN neural network controlled the autonomous CMU NAVLAB using just 30×32 images as input [70]. Robust obstacle avoidance was achieved by Lorigo et~al. [51] using 64×48 images. In contrast to this historical work, our approach is driven not by hardware

limitations by rather inspired by the limits of possibility, as in Torralba *et al.* [91, 92] and in Basu and Li [4], who argue that different resolutions should be used for different robotic tasks. Our work is unique in that we demonstrate autonomous navigation in unknown indoor environments using not only low-resolution images but also intermittent processing.

2.2 Vision based navigation – an overview

Typically using on-board computation and standard off the shelf hardware, mobile robots using multiple sensors have been developed for land, sea and aerial navigation and are deployed in the manufacturing, military, security, consumer and entertainment industries. Vision is powerful because it is inexpensive, non-intrusive and scalable. The various ways in which vision is used for navigation have been described in detail, by Desouza *et al.* [22]. Vision-based navigation systems can be classified as shown in Figure 2.1 which is a summary of [22]. This thesis aims to form a bridge between map-building systems and mapless systems, thus combining the goal of autonomous exploration and mapping.

2.2.1 Mapless navigation

Mapless navigation using vision predominantly uses primitive visual competencies like measurements of 2D motion (such a optical flow), structure from motion, independent motion detection, estimating time-to-contact and object tracking [22]. While some/all of these can and have been used to develop a wandering robot, many open points of research need to be mentioned. None of these have been tested before on low-resolution systems (as low as 32×24). All of these visual competencies are known to face problems in textureless environments. These competencies can be used

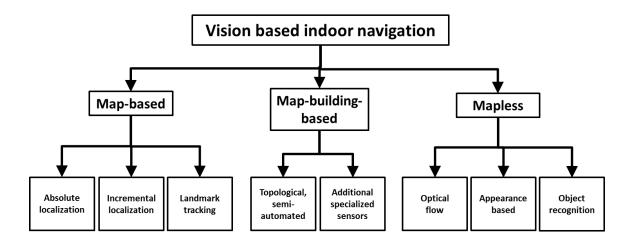


Figure 2.1: A taxonomy of approaches to vision-based navigation, summarizing [22]. for continuous navigation in a predictable path. At a point of discontinuity such as a corridor end, however, these competencies themselves do not provide a solution.

2.2.2 Map-based navigation

Map-based navigation systems are a complete solution to the goal-based navigation problem. The definition of landmarks is a vital necessity of such a system. Again, historically there have been two types of visual landmarks: Sparse feature based landmarks and higher level abstract landmarks.

• Sparse feature based landmarks: Some of the prominent landmarks used today to represent visual landmarks in SLAM based systems, are based on edges, rotation invariant features, or corners. These are in fact represented by the three popular visual landmark representation techniques: SIFT (Scale Invariant Feature Transform) [79], Harris Corners [25] or Shi-Tomasi feature points [84]. These have the advantage of being robust, scale invariant and sparse [39]. But again the important points to be noted are as follows. These representations

are computationally quite expensive. Some work has been done to develop real-time feature detectors, like real-time SLAM [21], GLOH [60] and SURF [6]. FAST [74, 75] is promising for high-speed, feature-based representations, but such approaches often leave little CPU time for other tasks and may not work well with textureless environments. These features work well in well-textured environments with high-resolution. In poorly textured environments with low resolution, sparse features are not robust enough. SIFT in particular is fairly sensitive to resolution and texture.

• High level abstract landmarks: Another way of representing landmarks is to use all of the pixels together like the entire image itself, or reduced pixel information. Template matching is a very simple, common yet powerful landmarks representation/matching technique. Histograms, color maps and other measures are also popular.

2.2.3 SLAM: Simultaneous Localization and Mapping

With regard to mapping, the recent developments in Simultaneous Localization and Mapping (SLAM) have been based primarily upon the use of range sensors [62, 72, 9]. A few researchers have applied this work to the problem of building maps using monocular cameras, such as in the vSLAM approach [37], which is a software platform for visual mapping and localization using sparse visual features. An alternate approach is that of Davison *et al.* [20, 19], who also use sparse image features to build 3D geometric maps.

In these visual SLAM techniques, either a complex matching process for a simple landmark representation [73] or a simple matching process for a complex landmark representation [79] is needed for robust robot localization. In indoor corridor

environments, however, the lack of texture poses a major obstacle to such an approach. Indeed, popular techniques such as the Scale Invariant Feature Transform (SIFT) [79] or other feature representations have difficulty in such cases. Moreover, the computationally demanding nature of these algorithms often leaves little room for additional processing, and their design requires higher resolution images.

2.2.4 Map-building based navigation

The whole task of map-building described in modern SLAM, visual or not, always has a manual/tele-operated phase [18, 78, 20]. It is important to note that in most map-building systems, the robot is controlled manually. Autonomous navigation is rare, and autonomous vision-based mapping is even more rare [22]. Notable initiatives include the work done by Matsumoto et al. [55], who used omnidirectional cameras with stereo and optical flow to control navigation, and Shah et al. [81], who implemented an autonomous navigation system using a calibrated fish eye stereo lens system. However, these approaches require specialized cameras. Similarly, autonomous vision-based navigation is rare, with many techniques requiring a training phase in which the robot is controlled manually [8, 13, 56, 57, 33]. As a result, efficient autonomous map building of indoor environments using a single off-the-shelf camera has remained an elusive problem.

Team ARobAS of INRIA have made a compelling statement in their annual report [87] about the incompleteness of SLAM. They state that the problem of explorative motion strategy of the robot (or reactive navigation) has rarely been a part of SLAM. They argue that autonomous navigation and SLAM cannot be treated separately and that a unified framework is needed for perception, modeling and control. Very few notable initiatives have completely automated the system for collecting the

data required to build a map while navigating. Robust perception is a basic necessity for a navigating robot that can be deployed in an environment without human intervention.

It is also important to distinguish our work from the large body of SLAM literature [89]. Simultaneous localization and mapping (SLAM) aims to produce a map of the environment while at the same time determining the robot's location within the map. Such approaches do not typically focus on autonomous exploration. One notable exception is the RatSLAM system [61], which is capable of robust autonomous exploration, mapping, localization, and navigation using a combination of vision, laser, sonar, and odometry sensors. RatSLAM is inspired by biological systems which demonstrate the ability to build and maintain spatial representations that are used as the basis of goal directed navigation throughout the lifetime of the organism. The localization and mapping algorithm is based on computational models of parts of the rodent's brain. The system built was a mobile robotic platform that is capable of mock delivery tasks in an office building. However even though vision is used in the mapping process, only lasers, sonars, and odometry are used to aid autonomous navigation around obstacles and straight line navigation. In contrast, our approach achieves more modest objectives but relies on vision alone.

Chapter 3

Estimating the Orientation in a Corridor

In order for a mobile robot to autonomously maneuver through an indoor office environment, one obvious parameter that must be estimated is the robot's orientation within the corridor. We propose to combine five complementary ways of estimating this value from low-resolution images: the entropy of the image, the symmetry as measured by mutual information, aggregate phase, vanishing points using self-similarity of the image, and the median of the bright pixels. The goal is to learn a mapping $f: I \to \theta$, where I is the low-resolution image and θ is the orientation of the robot with respect the primary axis of the corridor.

3.1 Entropy

We have found empirically that, as a general rule, entropy is maximum when the camera is pointing down the corridor. The reason for this (perhaps surprising) result is that such an orientation causes scene surfaces from a variety of depths to be visible, yielding an increase of image information at this orientation. In contrast, when the robot is turned so that it faces one of the side walls, the range of visible depths is much smaller and therefore the variety of pixel intensities usually decreases. A similar observation has been noted by other researchers in the context of using omnidirectional images [10, 23], but we show that the relationship between entropy and orientation holds even for standard camera geometries. In addition, we have found that the relationship is not significantly affected whether or not the walls are textured.

We exploit this property by dividing the image into overlapping vertical slices and computing the graylevel entropy of the image pixels in each slice. The horizontal coordinate yielding the maximum entropy is then an estimate of the orientation. More precisely, let us define a vertical slice of pixels centered at x as $C_{\omega}(x) = \{(x', y') : \frac{\omega}{2} \leq |x - x'| < \frac{\omega}{2} \}$, where ω is the width of the slice. If p(v; x) is the normalized histogram of pixel values in $C_{\omega}(x)$, then the graylevel entropy of the slice is given by $H(V; I, x) = -\sum_{v \in V} p(v; x) \log p(v; x)$. This is illustrated in Figure 3.1. The orientation estimate is then given by $f_1(I) = \psi(\arg\max_x H(V; I, x))$, where the function ψ converts from pixels to degrees. With a flat image sensor and no lens distortion, the horizontal pixel coordinate is proportional to the tangent of the angle that the projection ray makes with the optical axis. Since the tangent function is approximately linear for angles less than 30 degrees, we approximate this transformation by applying a scalar factor: $\psi(x) = \alpha x$, where the factor α is determined empirically.

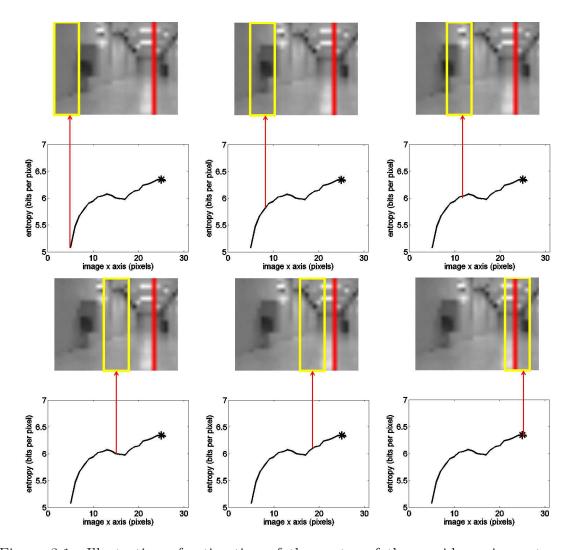


Figure 3.1: Illustration of estimation of the center of the corridor using entropy. The image is divided into 10 pixel-wide columns (yellow rectangle), and entropy is calculated for each column. In lexicographic order from top left, the entropy in each column increases, yielding a peak at the rightmost column corresponding to the corridor center. The success is due to the fact that the latter column contains orientation scene surfaces from a variety of depths, thereby increasing the information content.

3.2 Symmetry by mutual information

Symmetry is defined as the invariance of a configuration of elements under a group of automorphic transformations [101]. However, the exact mathematical definition is inadequate to describe and quantify the symmetries found in the natural world nor those found in the visual world. Zabradosky et al. [104] mention that even perfectly symmetric objects lose their exact symmetry when projected onto the image plane or the retina due to occlusion, perspective transformations, digitization, etc. Thus, although symmetry is usually considered a binary feature, (i.e. an object is either symmetric or it is not symmetric), we view symmetry as a continuous feature where intermediate values of symmetry denote some intermediate amount of symmetry [104]. Much of the work related to symmetry concerns symmetry detection (symmetry in the binary sense) as in [14, 86, 3, 83]. Very few noteworthy contributions exist that venture to measure the amount of symmetry in an image. Zabradosky et al. [104], Marola [54], Kanatani [36], van Gool [97] are some of the prominant authors in this respect. However all of these experiments associate symmetry with shape, which requires shape computation/comparison of some kind with respect to a discrete set. To the best of our knowledge a continuous measure of symmetry using low level image information (the raw image bits) in low resolution has not been developed before. We propose a new measure of symmetry using information theoretic clues.

Another property of corridors is that they tend to be symmetric about their primary axis. Various approaches to detecting and measuring symmetry have been proposed [104, 46, 3, 14]. However, in our problem domain it is important to measure the *amount* of symmetry rather than to simply detect axes of symmetry. One way to measure the amount of reflective symmetry about an axis is to compare the two regions on either side of the axis using mutual information. Mutual information is

a measure of the amount of information that one random variable contains about another random variable, or equivalently, it is the reduction in the uncertainty of one random variable due to the knowledge of the other. Mutual information has emerged in recent years as an effective similarity measure for comparing images [38, 76, 27]. As with entropy, for each horizontal coordinate x a column of pixels C(x) is considered, where we have dropped the ω subscript for notational simplicity. The column is divided in half along its vertical center into two columns $C_L(x)$ and $C_R(x)$. The normalized graylevel histograms of these two regions are used as the two probability mass functions (PMFs), and the mutual information between the two functions is computed:

$$MI(x) = \sum_{v \in \mathcal{V}} \sum_{w \in \mathcal{V}} p(v, w; x) \log \frac{p(v, w; x)}{p_L(v; x) p_R(w; x)},$$
(3.1)

where p(v, w; x) is the joint PMF of the intensities in both sides, and $p_L(v; x)$ and $p_R(w; x)$ are the PMFs computed separately of the intensities of the two sides. As before, the orientation estimate is given by $f_2(I) = \psi(\arg\max_x MI(x))$.

3.3 Aggregate phase

A third property of corridors is that the dominant intensity edges tend to point down the length of the corridor. Therefore, near the center of the corridor, the phase angles of these edges on the left and right sides will balance each other, yielding a small sum when they are added together. We compute the gradient of the image using a Sobel operator and retain only the phase $\phi(x, y)$ of the gradient at each pixel. For each horizontal coordinate x we simply add the phase angle of all the pixels in the vertical slice: $AP(x) = \sum_{(x,y) \in \mathcal{C}(x)} \phi(x,y)$. The orientation estimate is given by $f_3(I) = \psi(\arg\min_x AP(x))$. Phase angles overlaid on several example images are

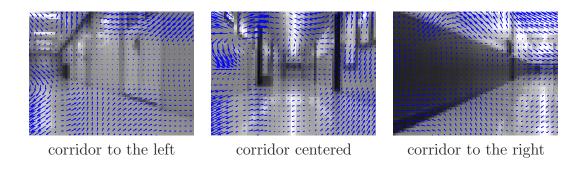


Figure 3.2: Gradient phase vectors overlaid on corridor images. From left to right: The center of the corridor is on the left side of the image, in the center of the image, and on the right side of the image. The phase vectors generally point toward the center of the corridor, so that in a vertical stripe near the center, the vectors balance each other.

shown in Figure 3.2.

3.4 Vanishing point using self-similarity

An additional property of corridors is the vanishing point, which is nearly always present in the image when the robot is facing down the corridor. Our approach is based on the work of Kogan et al. [41], who developed a novel self-similarity based method for vanishing point estimation in man-made scenes. The key idea of their approach, based upon the work of Stentiford [85], is that a central vanishing point (meaning a vanishing point that is visible in the image) corresponds to the point around which the image is locally self similar under scaling changes. See Figure 3.3. While Kogan et al. [41] use 1D cross-sections of the image for similarity matching using affine transformation and cross correlation, we instead shift the downsampled image across the original image and calculate the mutual information between the two windows. The point at which the mutual information between the two images is maximum yields a location for the downsampled image. The vanishing point is then found by intersecting the lines connecting the corners of the two images. Once we

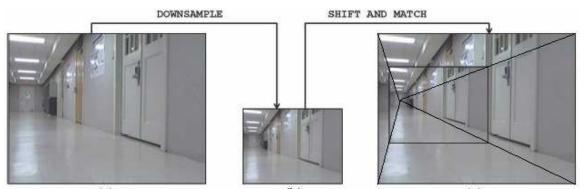


Figure 3.3: Vanishing point estimation from global self-similarity. (a) Original image of a corridor. (b) The image downsampled by a factor of two. (c) The downsampled image overlaid on the original image at the location of maximum self-similarity. The intersection of the lines connecting the corners of the two images yields the vanishing point. Normal resolution images are shown here only for display purposes, since the actual algorithm uses low-resolution 32×24 images.

find the vanishing point, we discard the y coordinate, retaining only the x coordinate because our goal is to determine the robot's orientation within the corridor. This leads to $f_4(I) = \psi(\hat{x})$, where (\hat{x}, \hat{y}) is the intersection of the corner-connecting lines.

Our self-similarity approach has several advantages over existing techniques: It is simple, computationally efficient, and yields good results even for low-resolution images. Traditional techniques [58, 71] involve clustering detected lines, which perform poorly in low-resolution images because lines are not easily detected in such images. A more recent approach by Kong et al. [44] uses Gabor filters to yield texture estimates, and an adaptive voting scheme allows pixels to decide the confidence of an orientation rather than relying upon explicit line detection. Not only is their approach much more computationally intensive than ours, but with indoor low-resolution images the results are less accurate. See Figure 3.4 for some examples.



Figure 3.4: Comparison between our vanishing point estimation approach (green circle) using self-similarity and that of Kong *et al.* [44] (red plus). Our approach is more robust to the scenario of low texture information which is common in indoor scenes.

3.5 Median of bright pixels

The ceiling lights, which are usually symmetric with respect to the main corridor axis, provide another important cue. Due to the low resolution of the image, it is not possible to analyze the shape of the lights, as in [15]. Moreover, sometimes the lights are not in the center of the corridor but rather on the sides. A simple technique that overcomes these difficulties is to apply the k-means algorithm [53] to the graylevel values in the upper half of the image, with k=2. The median horizontal position of the brighter of the two regions is calculated, yielding an estimate of the center of the corridor. (The use of median as opposed to mean prevents the result from being affected by specular reflections on either wall.) We have found this approach to be not only simpler, but also more accurate and more generally applicable, than the shapebased technique in [15]. Note that ceiling lights provide an added advantage over vanishing points because they are affected by translation, thus enabling the robot to remain in the center of the corridor while also aligning its orientation with the walls. As with the previous measure, the horizontal coordinate is transformed to an angle by applying the same scalar factor. Therefore, $f_5(I) = \psi(\text{med}\{x : (x, y) \in \mathcal{R}_{bright}\}),$ where \mathcal{R}_{bright} is the set of bright pixels. Some segmentation results are shown in Figure 3.5.

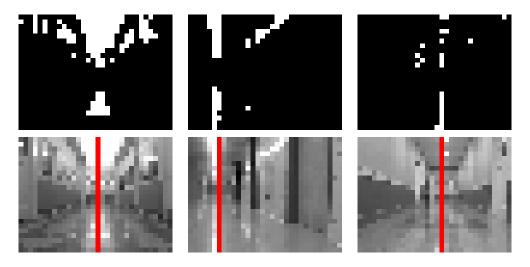


Figure 3.5: K-means segmentation results for ceiling lights, with k=2 (top), and corresponding estimate (red vertical line) of the center of the corridor bottom.

Chapter 4

Estimating the Distance to the End of a Corridor

The second state parameter to be estimated is the distance to the end of the corridor. To solve this problem, we combine three complementary measures: time-to-collision, Jeffrey divergence, and entropy.

4.1 Time-to-collision

Time-to-collision (TTC) is defined as the time it will take the center of projection of a camera to reach the opaque surface intersecting the optical axis, if the relative velocity between the camera and the surface remains constant. Traditional methods of computing TTC [1, 17] require computing the divergence of the estimated optical flow, which is not only computationally intensive but, more importantly, requires a significant amount of texture in the scene. To overcome these problems, Horn et al. [29] have recently described a direct method to determine the time-to-collision using image brightness derivatives (temporal and spatial) without any calibration,

tracking, or optical flow estimation. The method computes the TTC using just two frames of a sequence, filtering the output using a median filter, to yield a reliable estimate as the camera approaches the object. This method is particularly applicable to our scenario in which the robot approaches a planar surface by translating in a direction parallel to the optical axis, a scenario for which the algorithm achieves an extremely simple formulation. Given two successive image frames $I^{(1)}$ and $I^{(2)}$ taken at different times, the TTC is computed as

$$\tau(I^{(1)}, I^{(2)}) = \frac{-\sum_{x,y} (G(x,y))^2}{\sum_{x,y} G(x,y) I_t(x,y)},$$
(4.1)

where $G(x,y) = xI_x(x,y) + yI_y(x,y)$, I_x and I_y are the spatial derivatives of the image intensity function, and $I_t(x,y)$ is the temporal derivative. Normally, the summation would be computed over the desired planar object, but in our case we compute the sum over the entire image. Although the scene is not strictly planar when the robot is at the beginning of the corridor, we have found empirically that the TTC values are nevertheless higher at the beginning of the corridor, indicating that the method succeeds in estimate the TTC qualitatively even at larger distances. As the robot approaches the end of the corridor, the scene in the field of view becomes more planar, thereby increasing the accuracy of the estimated TTC. We transform the TTC to an estimate of the distance to the end by dividing the robot speed by it: $g_1(I^{(1)}, I^{(2)}) = s/\tau(I^{(1)}, I^{(2)})$, where s is the robot translational speed.

4.2 Jeffrey divergence

As the robot approaches the end of the corridor, the pixel velocities increase, thereby causing the image to change more rapidly. As a result, another way to estimate the distance to the end is to measure the distance between two images. A convenient way to compare two images is to measure the Jeffrey divergence [96], which is a symmetric version of the Kullback-Leibler divergence:

$$J(p,q) = \sum_{v \in \mathcal{V}} \left(p(v) \log \left(\frac{p(v)}{q(v)} \right) + q(v) \log \left(\frac{q(v)}{p(v)} \right) \right), \tag{4.2}$$

where p and q are the graylevel histograms of the two successive images $I^{(1)}$ and $I^{(2)}$, respectively, and the summations are over the entire image. There is an inverse relationship between the divergence and the distance, so we transform this value to an estimate of the distance to the end by subtracting a scaled version from a constant to keep the result non-negative: $g_2(I^{(1)}, I^{(2)}) = \beta_2 - \alpha_2 J(p^{(1)}, q^{(2)})$, where β_2 is the offset.

4.3 Entropy

It is also true that, as the robot approaches the end of the corridor, the entropy of the image increases more rapidly. An alternate way to estimate the distance to the end, then, is to compute the difference in entropy between consecutive image frames, which also has an inverse relationship with distance: $g_3(I^{(1)}, I^{(2)}) = \alpha_3/(H(V; I^{(1)}) - H(V; I^{(2)}))$, where α_3 is a scale factor.

Chapter 5

Filtering the estimates using a Kalman filter

In our previous work we estimated orientation using only the median of bright pixels and distance to the end of the corridor was largely determined by entropy [64]. In recent work we showed that a linear combination (weighted average) of five (orientation) and three (distance to the end) complementary measures is more effective for achieving success in multiple environments [65]. However we now show a state space representation of the variables to be estimated, namely orientation in the corridor (θ) and distance to the end (d). We show that a Kalman filter combining the measurements is most effective in this case, providing more reliable estimates over time than a simple weighted average.

5.1 Noise model development

In order to reduce the effects of noise that corrupts the measurements from the image, we need to set up a filter to remove/reduce the noise in the state space represented by orientation in the corridor and the distance to the end of the corridor. We know that the motion of the robot along a straight line in the corridor is linear and assuming that the noise is Gaussian, we can use a Kalman filter to achieve robust state estimation as shown in Appendix 2. Two major statistical properties are studied to analyze the noise characteristics and evaluate the noise models: the histogram and the autocorrelation function [32, 98]. Our goal of modeling a sensor system is to construct a probabilistic model using some commonly used random variables or processes. Additive White Gaussian Noise (AWGN) is a typical random process for this scenario. Since techniques relating AWGN are well-developed, analysis would be simplified if the sensor noise of interest is AWGN or can be approximated as such. By contrast, if the characteristics exhibited by the data are too complex to be modeled easily and model accuracy is less important, use of a typical random process or combinations of several of them are justifiable for rough approximation.

5.1.1 Histogram (estimation of Gaussian probability density function)

For a given single location, if multiple sensor readings are takes and the measurements are analyzed, the histogram of the residuals of the measurements gives us an approximation of the probability density of the noise involved. Jenkins *et al.* [32] showed that if the histogram approximates a bell shaped curve, then the noise characteristics can be considered Gaussian.

5.1.2 Sample autocorrelation function (White Noise)

The autocorrelation function describes the second order statistics of a random process. It is used here because it gives a visual picture of the degree to which samples in the process are dependent upon each other as a function of the separation between points in the data series. From Jenkins [32], the autocovariance function (ACVF) estimates of a discrete time series could be defined as following: If the observations X_1, X_2, X_n are a discrete set of values corresponding to multiple measurements for the same actual (unobservable) value, the discrete autocovariance estimate is:

$$c_{xx}(k) = \frac{1}{N} \sum_{i=1}^{N-k} (x_i - \bar{x})(x_{i+k} - \bar{x}), k = 0, 1, ...N - 1$$
 (5.1)

where $\bar{x} = \frac{1}{N} \sum_{i=1}^{N} x_i$. Estimates of the autocorrelation function (ACF), also called sample ACF, are obtainable by dividing the above ACVF estimates by the estimate of the variance, which is

$$r_{xx}(k) = \frac{c_{xx}(k)}{c_{xx}(0)} \tag{5.2}$$

The ACF of an ideal white Gaussian process is always zero. So ACF of a set of residual test data which settle down at zero or are close to zero can be considered/modeled as white Gaussian noise.

5.1.3 Noise model for orientation measurements

We estimate the noise model for the five orientation measurements, median of ceiling lights, maximum entropy, maximum symmetry, vanishing points and aggregate phase. In each case we show that the histogram of the residual noise for a few token well separated orientation measurements closely match the Gaussian. We also show that the ACF approaches zero in each case, establishing the noise in each case to be AWGN.

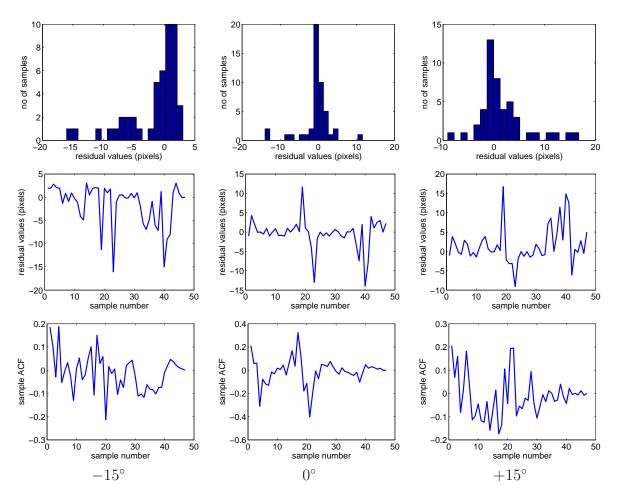


Figure 5.1: Showing histogram (TOP), residual noise(MIDDLE), ACF (BOTTOM) for three token orientations in the corridor $-15^{\circ}(LEFT)$, $0^{\circ}(CENTER)$, $+15^{\circ}(RIGHT)$.

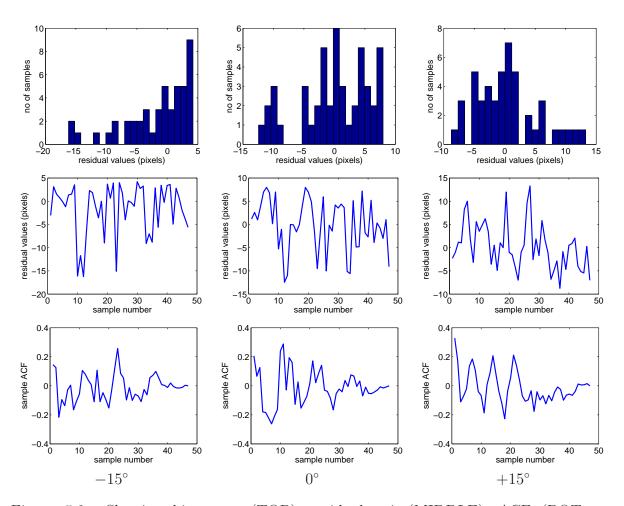


Figure 5.2: Showing histogram (TOP), residual noise(MIDDLE), ACF (BOTTOM) for three token orientations in the corridor $-15^o(\text{LEFT})$, $0^o(\text{CENTER})$, $+15^o(\text{RIGHT})$.

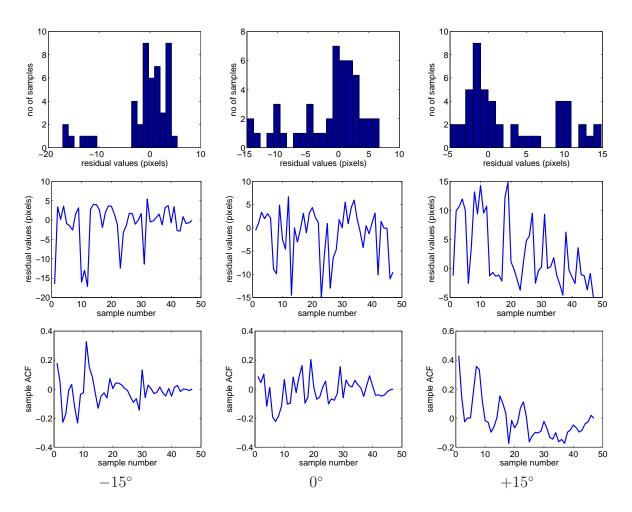


Figure 5.3: Showing histogram (TOP), residual noise(MIDDLE), ACF (BOTTOM) for three token orientations in the corridor $-15^{\circ}(LEFT)$, $0^{\circ}(CENTER)$, $+15^{\circ}(RIGHT)$.

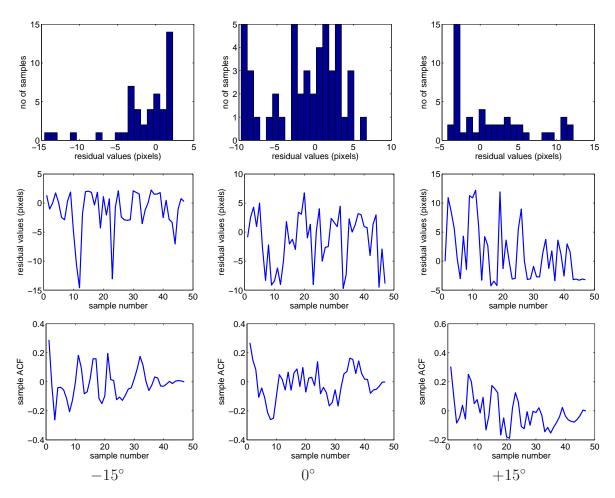


Figure 5.4: Showing histogram (TOP), residual noise(MIDDLE), ACF (BOTTOM) for three token orientations in the corridor $-15^{\circ}(LEFT)$, $0^{\circ}(CENTER)$, $+15^{\circ}(RIGHT)$.

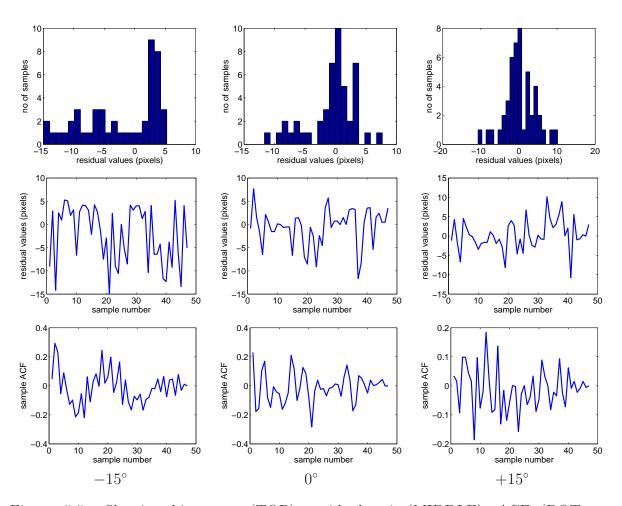


Figure 5.5: Showing histogram (TOP), residual noise (MIDDLE), ACF (BOTTOM) for three token orientations in the corridor $-15^{\circ}(\text{LEFT}),~0^{\circ}(\text{CENTER}),~+15^{\circ}(\text{RIGHT}).$

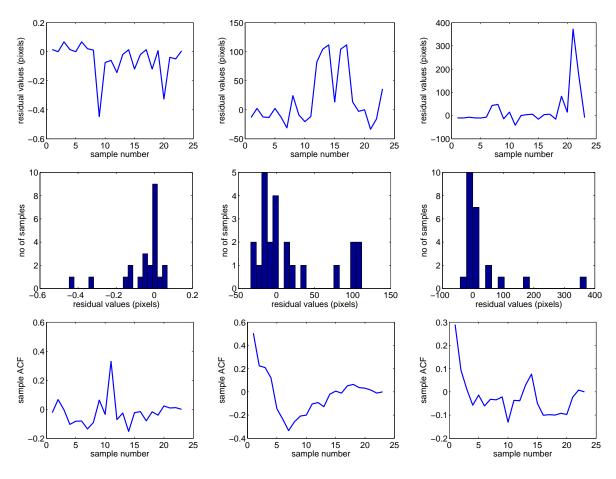


Figure 5.6: Showing histogram (TOP), residual noise(MIDDLE), ACF (BOTTOM) for entropy(LEFT), Jeffrey divergence(CENTER), time-to-collision(RIGHT).

5.1.4 Distance to the end

We estimate the noise model for the three distance to end measurements, entropy, Jeffrey divergence and time-to-collision. In each case we show that the histogram of the residual noise for a few token well separated orientation measurements closely match the Gaussian. We also show that the ACF approaches zero in each case, establishing the noise in each case to be AWGN.

5.2 State space variables and parameters for the Kalman filter

The state is defined by local variables θ and d. While most typical robotic systems work on a x, Y, θ systems, for simplicity and keeping in view the minimalistic design, we use only two. Also because we directly use the estimated θ for setting the rotational velocity, and because we are not measuring or controlling the lateral position directly (the robot being non-holonomic). Also the robot travels at a constant velocity which is set to zero when the distance to the end estimated as d falls below a threshold (generally 1.5 m away from the end of the wall).

5.2.1 State

$$X = \begin{bmatrix} \theta \\ \dot{\theta} \\ d \\ \dot{d} \end{bmatrix} \tag{5.3}$$

where θ is the robot orientation in the corridor and d is the distance to the end of the corridor. $\dot{\theta}$ and \dot{d} are corresponding velocities.

$$d_{t+t} = d_t + \dot{d}_t T + 0$$

$$\theta_{t+1} = \theta_t + \dot{\theta}_t T + 0$$

$$\dot{d}_{t+1} = \dot{d}_t + \eta_d \text{ where } \eta_d \in \mathcal{N}(0, \dot{\sigma}_d)$$

$$\dot{\theta}_{t+1} = \dot{\theta}_t + \eta_\theta \text{ where } \eta_\theta \in \mathcal{N}(0, \dot{\sigma}_\theta)$$
(5.4)

$$X = \begin{bmatrix} \theta \\ \dot{\theta} \\ d \\ \dot{d} \end{bmatrix} = \begin{bmatrix} 1 & T & 0 & 0 \\ 0 & 1 & 0 & 0 \\ 0 & 0 & 1 & T \\ 0 & 0 & 0 & 1 \end{bmatrix} \begin{bmatrix} \theta \\ \dot{\theta} \\ d \\ \dot{d} \end{bmatrix} + \begin{bmatrix} 0 \\ \eta_{\theta} \\ 0 \\ \eta_{d} \end{bmatrix}$$
(5.5)

$$X_{t+1} = \Phi X_t + U_t \tag{5.6}$$

where Φ is called the state transition matrix and U_t stands for the random acceleration in the time period T.

5.2.2 Measurements

$$Y = \begin{bmatrix} c_1 & c_2 & c_3 & c_4 & c_5 & z_1 & z_2 & z_3 \end{bmatrix}^T \tag{5.7}$$

where c_1 , c_2 , c_3 , c_4 , c_5 stand for the horizontal position orientation in the image corresponding to the center of corridor by using median of ceiling lights, maximum entropy, maximum symmetry, vanishing point using self-similarity, and aggregate phase. z_1 , z_2 and z_3 correspondingly stand for distance between two consecutive images that correspond to the distance to the end estimated from time-to-collision (s), Jeffrey divergence (bits/pixel) and entropy difference (bits/pixel).

$$c_i = \frac{\theta}{k_i} + \eta_{c_i} \text{ where } i = (1..5) \text{ and } \eta_{c_i} \in \mathcal{N}(0, \sigma_{c_i})$$

 $z_i = \frac{d}{l_i} + \eta_{z_i} \text{ where } i = (1..3) \text{ and } \eta_{z_i} \in \mathcal{N}(0, \sigma_{z_i})$

$$(5.8)$$

where $k_1, k_2, k_3, k_4, k_5, l_1, l_2, l_3$ are all constants estimated from a linear fit between the measurements and the ground truth orientation θ described in the previous section.

$$\begin{bmatrix} c_{1} \\ c_{2} \\ c_{3} \\ c_{4} \\ c_{5} \\ z_{1} \\ z_{2} \\ z_{3} \end{bmatrix} = \begin{bmatrix} \frac{1}{k_{1}} & 0 & 0 & 0 \\ \frac{1}{k_{2}} & 0 & 0 & 0 \\ \frac{1}{k_{3}} & 0 & 0 & 0 \\ \frac{1}{k_{5}} & 0 & 0 & 0 \\ 0 & 0 & \frac{1}{l_{1}} & 0 \\ 0 & 0 & \frac{1}{l_{2}} & 0 \\ 0 & 0 & \frac{1}{l_{3}} & 0 \end{bmatrix} \begin{bmatrix} \theta \\ \dot{\theta} \\ \dot{d} \\ \dot{d} \end{bmatrix} + \begin{bmatrix} \eta_{\sigma_{c_{1}}} \\ \eta_{\sigma_{c_{2}}} \\ \eta_{\sigma_{c_{3}}} \\ \eta_{\sigma_{c_{5}}} \\ \eta_{\sigma_{z_{1}}} \\ \eta_{\sigma_{z_{2}}} \\ \eta_{\sigma_{z_{3}}} \end{bmatrix}$$

$$(5.9)$$

$$Y_t = MX_t + N_t \tag{5.10}$$

where M is the observation matrix which contains the constants corresponding to the linear fit for the different measurements as shown in equation (5.9).

5.2.3 Noise

$$R = \begin{bmatrix} \sigma_{c1}^{2} & 0 & 0 & 0 & 0 & 0 & 0 & 0 \\ 0 & \sigma_{c2}^{2} & 0 & 0 & 0 & 0 & 0 & 0 \\ 0 & 0 & \sigma_{c3}^{2} & 0 & 0 & 0 & 0 & 0 \\ 0 & 0 & 0 & \sigma_{c4}^{2} & 0 & 0 & 0 & 0 \\ 0 & 0 & 0 & 0 & \sigma_{c5}^{2} & 0 & 0 & 0 \\ 0 & 0 & 0 & 0 & \sigma_{z1}^{2} & 0 & 0 \\ 0 & 0 & 0 & 0 & 0 & \sigma_{z2}^{2} & 0 \\ 0 & 0 & 0 & 0 & 0 & 0 & \sigma_{z3}^{2} \end{bmatrix}$$

$$(5.11)$$

The observation noise covariance matrix is given by R and the values in this matrix are obtained from the residual variances from the noise model developed in

the Section 5.1.2.

$$Q = \begin{bmatrix} 0 & 0 & 0 & 0 \\ 0 & \sigma_{u_{\theta}}^{2} & 0 & 0 \\ 0 & 0 & 0 & 0 \\ 0 & 0 & 0 & \sigma_{u_{d}}^{2} \end{bmatrix}$$

$$(5.12)$$

The dynamic noise covariance matrix is given by Q which corresponds to the random acceleration in the system, where $\sigma_{u_{\theta}}^{2}$ and $\sigma_{u_{d}}^{2}$ represent the dynamic noise in the rotational and translational velocities of the robot respectively.

These parameters were plugged in the Kalman filter equations described in Appendix 2 to achieve state space filtering.

5.3 Kalman filter in operation

Based on the noise models, variances of measurement noise and the Kalman filter model shown in the previous sections, we now show the working of the Kalman filter model on sample sequences collected from three corridors for orientation and distance to end estimations. In Appendix 2, we show the equations for real-time operation of the Kalman filter. We recorded a set of images along three corridors in three buildings (Riggs, Lowry and Freeman) (with the Logitech pro 4000 webcam) along with ground truth measurements using a SICK LMS-291 scanning laser. Deliberate noise was introduced by randomly changing the orientation in each case. For each image all the eight (5 orientation + 3 distance to end) measurements were obtained. These measurements were plugged into the Kalman filter equations described in the previous section and Appendix 2, to arrive at the state estimations. Figure 5.7 shows the results of the Kalman filter based orientation estimation for the three corridor

$1/k_1 =$	-0.35	$\eta_{\sigma_{c_1}} =$	16.1	$\sigma_{c_1}^2 =$	15
$1/k_2 =$	-0.41	$\eta_{\sigma_{c_2}} =$	16.7	$\sigma_{c_2}^2 =$	31
$1/k_3 =$	-0.29	$\eta_{\sigma_{c_3}} =$	16.08	$\sigma_{c_3}^2 =$	31
$1/k_4 =$	-0.22	$\eta_{\sigma_{c_4}} =$	16.61	$\sigma_{c_4}^2 =$	30
$1/k_5 =$	-0.30	$\eta_{\sigma_{c_5}} =$	14.75	$\sigma_{c_5}^2 =$	57
$1/l_1 =$	-0.0001	$\eta_{\sigma_{z_1}} =$	0.9	$\sigma_{z_1}^2 =$	0.24
$1/l_2 =$	-0.022	$\eta_{\sigma_{z_2}} =$	56	$\sigma_{z_2}^2 =$	8350
$1/l_3 =$	-0.0064	$\eta_{\sigma_{z_3}} =$	40.03	$\sigma_{z_3}^2 =$	8350

Table 5.1: Parameter values for the Kalman filtered estimated from the collected data and the noise model development

sequences.

5.3.1 Initialization of the Kalman filter

Initial values of the state and the parameters for tuning the Kalman filter are presented as follows.

$$X_{0,0} = \begin{bmatrix} 0 \\ 0 \\ 15 \\ -0.4 \end{bmatrix}$$
 (5.13)

, where the initial value of θ is 0 because initially the robot is oriented straight towards the center of the corridor. The initial value of d is set to some arbitrary large value 15m here for convenience, because the distance reduces as the robot approaches the end of the corridor and is expected to reach 0 at the end of the corridor. The velocities are set to be 0 for rotation and -0.4m/s translation. The values for M and N are as follows obtained from linear fits to the data collected during testing (See Section 8.1). The values for R, the observation noise covariance matrix, are obtained from the variances of the

Values from Table 5.1 are to be plugged into Equations (5.9) and (5.11). The

tuning of the filter is achieved by changing the values of $\sigma_{u_{\theta}}$ and $\sigma_{u_{d}}$ till the results are optimal. The values obtained were $\sigma_{u_{\theta}} = 0.03$ and $\sigma_{u_{d}} = 4000$. The value of T (time step) was set to be 0.06s for all our experiments. The low frame-rate is because of the SICK laser (ground truth sensor), which requires a large delay between captures for synchronization.

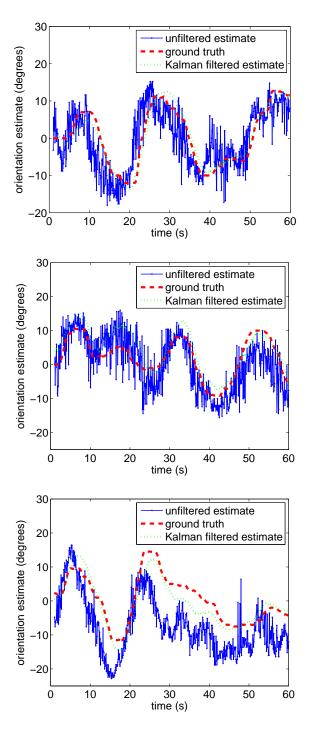


Figure 5.7: Orientation estimation for sequences of images collected in three corridors. In each case, the unfiltered measurements (linear weighted average of the five measurements), (blue solid) are shown along with the ground truth (red dashed) and the Kalman filtered estimate (green dotted).

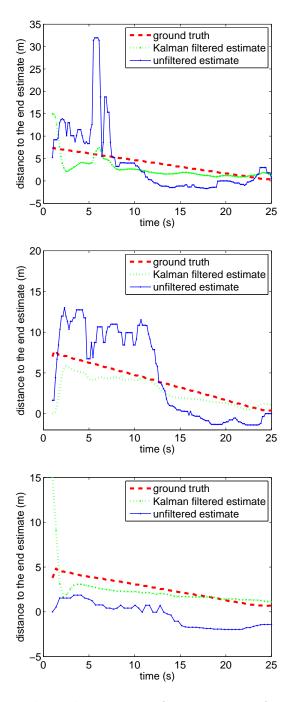


Figure 5.8: Distance to the end estimation for sequences of images collected in three corridors. In each case, the unfiltered measurements (linear weighted average of the five measurements), (blue solid) are shown along with the ground truth (red dashed) and the Kalman filtered estimate (green dotted).

Chapter 6

Corridor Junction Classification

6.1 Junction classification from monocular images

Apart from determining the orientation and distance to the end of the corridors for reactive navigation in unknown environments, we also show that image entropy alone can be used to detect new corridors at a junction and to classify the junction based on the information. The procedure followed for this experiment is as follows. The robot was mounted with a SICK LMS-291 laser scanner, and a Logitech QuickCam 4000 webcam and made to turn 360° at various types of indoor corridor junctions (dead end (D), middle (M), L-junction (L), T-junction (T), cross-junction (X)). Images were collected for junctions in 9 different corridors in 6 different buildings (Sirrine, Lowry, Freeman, Rhodes, Riggs and EIB). The robot was rotated at a speed of 2 degrees per second, and data was stored at the rate of 0.5 Hz, leading to densely sampled data approximately 1 degree apart. The laser provided depth readings in a 180-degree horizontal plane in increments of 1 degree, leading to 180 laser depth readings per sample time. Only the reading corresponding to) degrees was considered for depth after smoothing. The image entropy is plotted along with

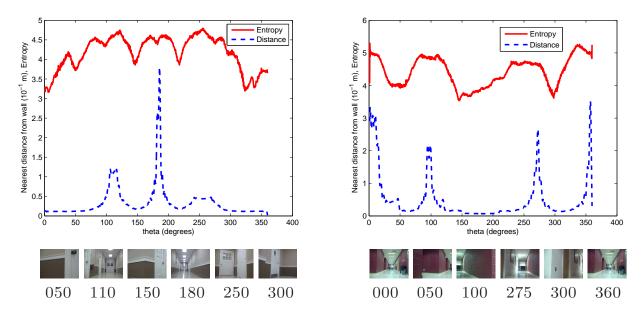
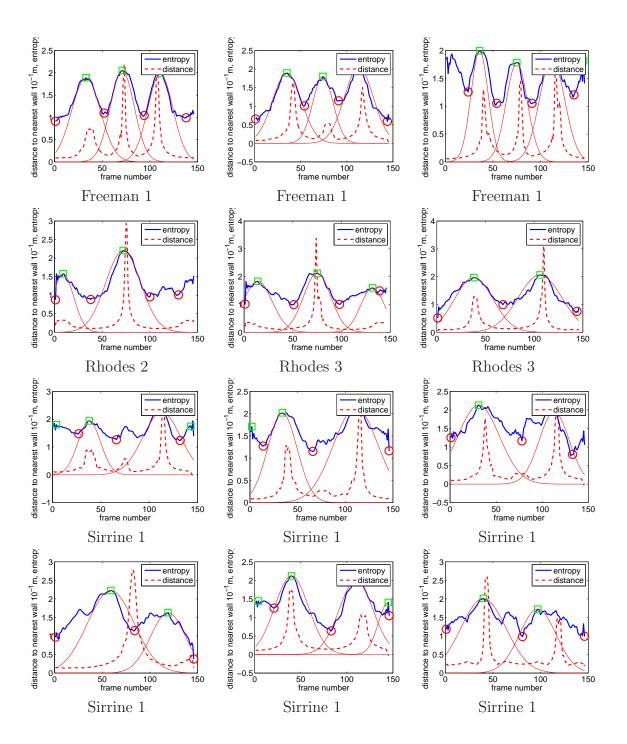


Figure 6.1: Top: Entropy (red solid line) and distance (blue dashed line) as the robot turned at a corridor T-junction in three different corridors. Distance was measured using a SICK scanning laser. BOTTOM: Images of the corridor approximately showing the orientation with respect to the depth values corresponding to them above.

the actual depth readings from the laser scanner. See Figure 6.1.

For each 0 to 360 degree sequence, the entropy values are treated as a onedimensional vector. It is smoothed using a Gaussian filter and is convolved with the derivative of a Gaussian. Boundaries are pruned and central zero-crossings are obtained for peaks and valleys in the 1-D signal from the convolved derivative. Amongst multiple close peaks/valleys detected, only the highest peak or lowest valley is chosen, and the rest is discarded, thus enforcing a minimum threshold distance between two peaks or valleys. In every signal, the number of peaks and the approximate angle between them is extracted to arrive at the type of junction. The signal between two valleys is taken and the mean (μ) and standard deviation (σ) are calculated. Gaussians are fitted at each of the peaks using this information. The detected peaks and fitted Gaussians for several corridors are shown in Figure 6.1.



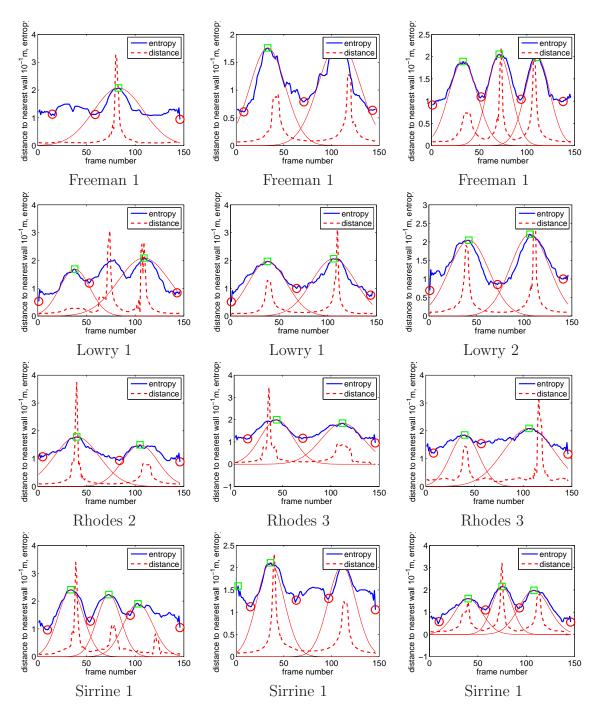


Figure 6.2: Corridor classification: Example junctions with Gaussian mixture models overlaid on the entropy peaks. Entropy as seen is powerful in itself to determine corridor depth when the depth change (due to structure) is significant. The green squares and red circles correspond to the detected peaks and valleys, respectively.

6.2 Junction classification from omnidirectional images

Catadioptric sensors have an advantage over monocular cameras (even though they are specialized) because they provide the robot with a 360° field of view thereby giving more abundant and rich information, which can be exploited in different ways for navigation [10]. The unwrapping of the image so obtained to a 1-D panaromic stack is convenient for analysis. See some example corridor images in Figure 6.4. Bonev et al. [10] have previously shown that entropy is powerful for determining open corridors in omnidirectional images. We however have previously independently shown that this works for standard monocular images in low-resolution. We show some examples in Figure 6.2 that strengthens the hypothesis in [10]. We have also shown in the previous section that the entropy peaks can be used to determine junction types in corridors. We show that the same technique can be applied to omnidirectional images to determine corridor junction types based on entropy peaks detected. Some examples are shown in Figure 6.5.

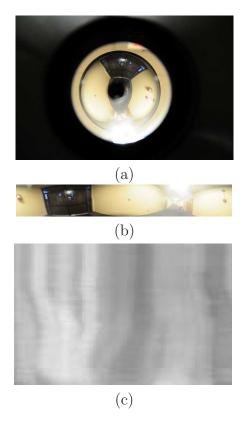


Figure 6.3: (a): Omnidirectional image of a corridor. The image was downsampled to 164×24 before processing(b):1-D panaromic rectified image. (c):The entropy map of the 1-D panaromic stack of a sequence of images along the same corridor. Entropy was calculated for each column (10 pixel wide) in the gradient magnitude image. Dark tones correspond to low entropy and light tones correspond to high entropy.

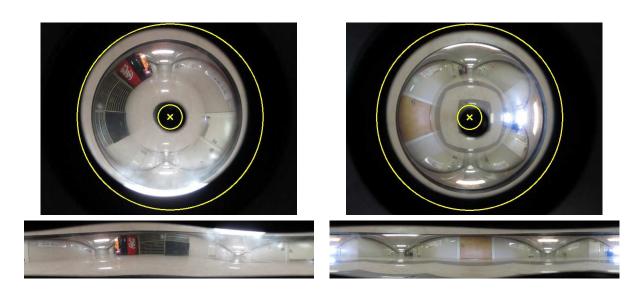
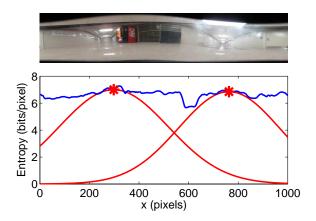


Figure 6.4: Sample omnidirectional images obtained with a camera and a hyperbolic mirror (TOP) and the rectified panaromic images (BOTTOM).



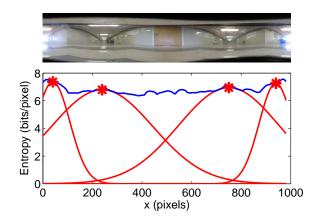


Figure 6.5: The entropy peak detection method used for monocular images works well on (unwrapped) omnidirectional images. The entropy values are smoothed using a Gaussian filter and are convolved with the derivative of a Gaussian. Boundaries are pruned and central zero-crossings are obtained for peaks (red asterisk) and valleys in the 1-D signal from the convolved derivative. Amongst multiple close peaks/valleys detected, only the highest peak or lowest valley is chosen, and the rest are discarded, thus enforcing a minimum distance between two peaks or valleys. The signal between two valleys is taken and the mean (μ) and standard deviation (σ) are calculated. Gaussians are fitted at each of the peaks using this information, shown as red solid curves.

Chapter 7

Estimating Corridor Geometry for Navigation

We present a minimalistic representation of the corridor geometry using low-resolution images for autonomous mobile robot navigation. We show a combination of percepts, orientation line and wall-floor boundary, to result in a three-line representation intersecting at the vanishing point. The orientation line can be used to keep the robot oriented along the corridor and the wall-floor boundaries can be used to keep the robot away from the walls (lateral limit). We also show that this representation can be achieved consistently across different resolutions from 320×240 to 16×12 with very little loss of accuracy.

7.1 Minimalistic corridor geometry

7.1.1 Estimating the orientation line

The orientation line is estimated using three of the above describes methods (maximum entropy, median of ceiling lights and maximum symmetry) for reasons

of simplicity. At standard resolution (320×240) , the calculation of the median of ceiling lights is corrupted by reflections. To solve this problem, we add an additional constraint using local contrast [95] along with k-means to segment the bright pixels. Only if local contrast exceeds a threshold, the pixels are considered to be from a light source. See Appendix 3 for details. It can be seen from Figure 7.1 that the effect of reflections are avoided to a great extent using this method. However, in low-resolution images the effect of the method is negligible.

The maximum symmetry and maximum entropy based orientation estimations however, remain the same. We combine the estimates as a weighted average: $f(I) = \alpha_l(I)f_l(I) + \alpha_h(I)f_h(I) + \alpha_s(I)f_s(I)$. Because of the reliability of the bright pixels, we set $\alpha_l = 0.8$, $\alpha_h = \alpha_s = 0.1$. An example result obtained for different resolutions is shown in Figure 7.2.

7.1.2 Estimating the wall-floor boundary

We adapt the floor segmentation method introduced by Li and Birchfield [49] which has been shown to be successfully robust to reflections on the floor. For the seven different resolutions, we compute the minimum acceptance length of the horizontal line segments l_h as $l_h = \ln \eta d$, where $d = \sqrt{w^2 + h^2}$ is the length of the diagonal of the image, w and h are the width and height of the image, respectively, and $\eta = 5$ is a scaling factor.

According to the floor segmentation method [49], there are three different scores (structure score, homogeneous score, and bottom score) that contribute to the final wall-floor boundary detection. When applying the method to different resolutions, we notice the structure score always shows the best accuracy while the bottom score always fails when decreasing the resolution. Therefore, we adapt the weights

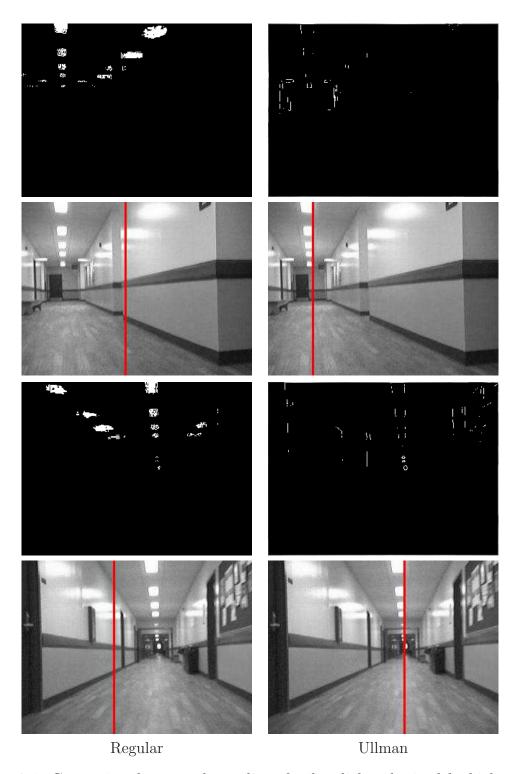


Figure 7.1: Comparison between the median of ceiling lights obtained for high resolution images using regular k-means and that by applying the local contrast threshold (described by Ullman [95]).

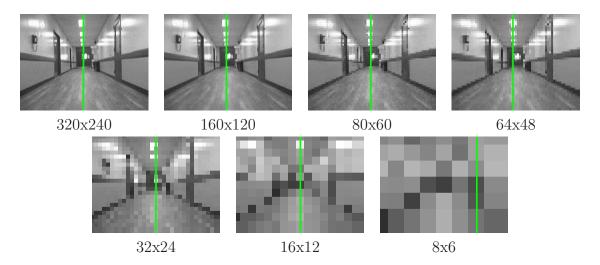


Figure 7.2: The orientation line estimate (vertical green line) for the images shown in Figure 1.1. Down to a resolution of 16×12 , the results remain essentially unchanged. Only at the lowest resolution of 8×6 is the technique unable to recover the orientation line accurately.

for the three scores according to the resolution so that the $\Phi_{total}(\ell_h)$ is relatively high for line segments near the wall-floor boundary. At the same time, when combining with the orientation line, we compute the intersection of the orientation line and the wall-floor boundary, which is considered as the vanishing point. Then we apply the line-fitting algorithm to both half wall-floor boundaries separated by the vanishing point. Using the slopes and the computed vanishing point, it is easy to find the two terminal points on the image border. Finally, we connect the vanishing point, two terminal points, as well as the orientation line and obtain the structure of the corridor. The sample results are shown in Figure 8.12 and the second row of Figure 7.4.

7.2 Minimalistic corridor reconstruction

7.2.1 Orientation line in the corridor

Estimating the pose of the robot or the orientation line of the robot in a typical indoor corridor is one of the necessary tasks for robot exploration/navigation. While many authors have contributed to this work, by estimating vanishing points in a corridor, [80, 7, 58, 71], the emphasis is on clustering detected lines, which perform poorly in low-resolution and textureless images because lines are not easily detected in such images. A more recent approach by Kong et al. [43] approaches the problem similarly but uses texture orientation rather than explicit line detection. In their approach, Gabor filters yield texture estimates, and an adaptive voting scheme allows pixels to decide the confidence of an orientation. However we show that not only is our method better suited for indoor images in low-resolution, but is also much faster. See Section 7.2.3.

7.2.2 Width of the corridor

The distance between the two end-points in the wall-floor boundary yields the width of the corridor (in pixels). We use a homography obtained during a calibration process to transform to world coordinates. The process is briefly illustrated in Figure 7.3. A square pattern on the floor and the corresponding real-world dimensions were used to obtain a homography between the image plane and the top-down view of the corridor. The homography was applied to the end points of the wall-floor boundary to obtain the top-down view of the reconstructed corridor.

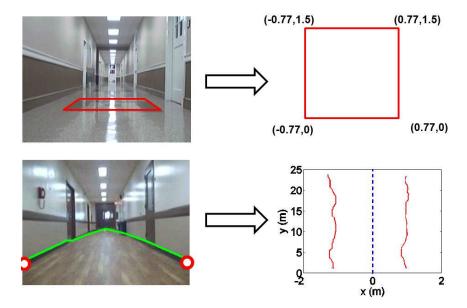


Figure 7.3: Top: A square with top-down ground truth world measurements (right) projects onto the image as a quadrilateral on the floor (left). The four points are sufficient for estimating a homography between the image and the top-down view of the corridor. Bottom: The homography is then applied to the end points of the wall-floor boundary to reconstruct the top-down view of the corridor. Shown on the right is a plot of such top-down coordinates (red dots) as the robot drives along a straight path (blue dashed line).

7.2.3 Lateral position in the corridor

The position of the orientation line with respect to the wall-floor boundaries will give the lateral position in the corridor. The top down dimensions of the reconstructed corridor gives us the distance from the center to the left wall and to the right wall. This can be used to obtain the lateral position of the robot in the corridor. The center of the corridor is assumed to be zero. For ground truth comparisons, the laser span readings were converted from polar to Cartesian to give a top-down measurement of the corridor at every instance of the image collection. Several examples are shown in Figure 8.13.

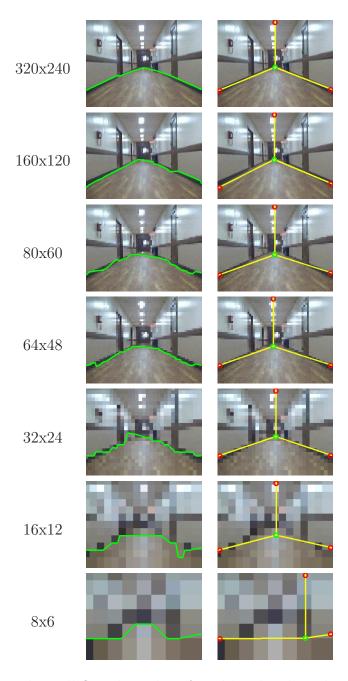


Figure 7.4: LEFT: The wall-floor boundary found by the algorithm described in [49] for the different resolution images of Figure 1.1. The accuracy degrades slightly until the resolution of 32×24 , after which the errors become more pronounced. RIGHT: The three-line model estimate of the corridor found by combining the orientation line with the wall-floor boundary, on the same images.

Chapter 8

Experimental Results

To test the approaches shown for solving the first problem (estimating the orientation and distance to the end), we analyze the accuracy of the various individual measures for the orientation and distance to the end. Then we describe the combined system and evaluate its performance exploring several unknown environments. For the second problem (corridor classification) we show the classification results for different buildings with different junction types. We also evaluate the classifier performance for the parameters used. For the third problem (minimalistic corridor geometry), we show orientation line estimated and wall-floor boundaries for different corridor across different resolutions. We then show a combined system with the three-line representation for all the resolutions. We evaluate the performance with respect to ground truth measurements and show the error for each resolution tested on.

8.1 Orientation along the corridor

We collected data for 10 unique corridors in 5 different buildings on our campus, shown in Figure 8.1. Multiple corridors were used for the same building only



Figure 8.1: 10 distinct corridors in 5 different buildings. The inset shows the 32×24 downsampled version, upsampled to make it more visible. In lexicographic order, the corridors are Riggs-0, Riggs-1, Riggs-2, Riggs-3, Rhodes-4, Sirrine-0, Sirrine-2, Freeman-0, Lowry-0, Lowry-2, where the number indicates the floor.

when they were located on different floors and exhibited varying appearances. For every corridor, at equally spaced 15 feet intervals along the corridor we rotated the robot from -20 degrees to +20 degrees while collecting odometry data, laser readings, and images. The equipment used was an ActivMedia P3AT mobile robot, a SICK LMS-291 laser, and a forward-facing Logitech QuickCam Pro 4000 webcam. The robot was rotated at a speed of 2 degrees per second, and data was stored at the rate of 0.5 Hz, leading to densely sampled data approximately 1 degree apart. The laser provided depth readings in a 180-degree horizontal plane in increments of 1 degree, leading to 180 laser depth readings per sample time. The peak of these depth laser readings, after smoothing, was used to estimate the ground truth orientation, except for one corridor containing large specular surfaces (Lowry-0), where the heading was obtained from the odometry readings.

Figure 8.2 shows the orientation estimates of the five different measures on six example images from different corridors and buildings. For each image, the vertical red line indicates the estimate of the corridor centerline. There is in general wide agreement between the various measures, and their error with respect to ground truth is generally less than about 5 degrees. Overall, the median of the bright pixels

yields the most accurate estimate, with the accuracy from entropy being only slightly degraded. The other three techniques also produce good results, but their accuracy is noticeably less. From the plots below, it can also be seen that the median of the bright pixels yields a very sharp peak compared with the other measures.

To determine the broad applicability of the approach, Figure 8.3 shows the results of the five measures on the database. Half of the data was used for developing algorithm parameters, so these results are shown for the other half of the database. The error bars show the range $\pm 2\sigma$ capturing 95% of the data, where σ is the standard deviation of the error. As can be seen, the error for entropy is generally less than 10 degrees, the error for bright pixels is less than 5 degrees, and the error for the other techniques is less than approximately 15 degrees. For entropy and bright pixels, the error does not vary significantly across headings, while for the other three measures the error varies widely.

For driving a robot down the center of the corridor, the most important information is whether the orientation estimate is in the correct direction. In other words, the estimate should tell the robot to turn right when it is pointing to the left, and it should tell the robot to turn left when it is pointing to the right. Figure 8.4 shows the percentage of locations in which each of the five measures computes the correct sign for the orientation, with the center of the image defined as the zero heading. Again, outside a 5- to 10-degree range around the center of the corridor, both the entropy and bright light measures nearly always produce the correct direction.

8.2 Distance to the end of the corridor

For the same 10 corridors mentioned earlier, we drove the robot down the corridor three times: down the center of the corridor, down the left side (1.5 feet

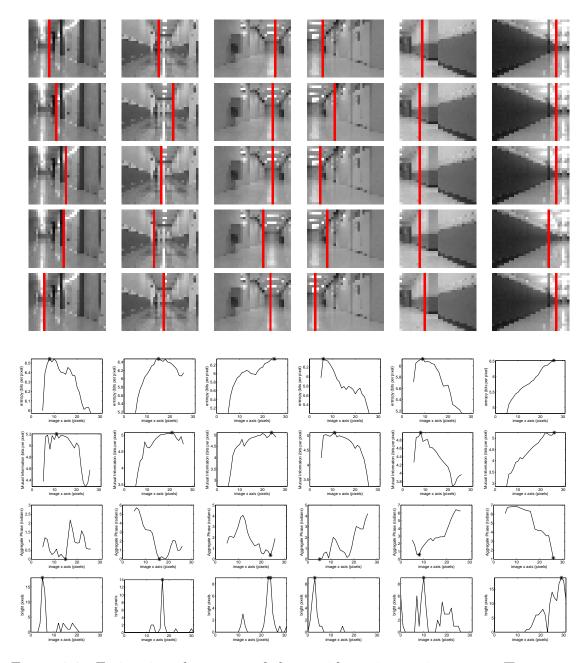


Figure 8.2: Estimating the center of the corridor using various cues. Top Rows: Six example tiny corridor images, with the pixel column corresponding to the center of the corridor overlaid for each of the five different methods: entropy, symmetry, aggregate phase, vanishing point, and bright pixels. Bottom Rows: Plots of the function computed for four of these measures — No plot for vanishing point is shown, since the technique directly produces an estimate.

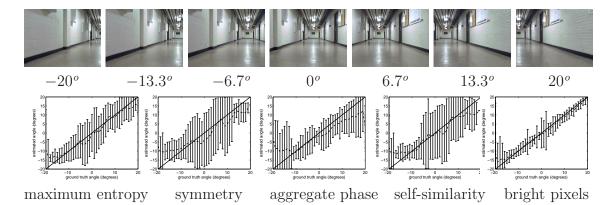


Figure 8.3: Top: Sample images from the orientation experiment in one corridor. Bottom: Orientation estimate plots for the five measures on the database. Each plot shows, for each angle of the robot, the mean estimated angle across the database along with error bars indicating indicates $\pm 2\sigma$, where σ is the standard deviation. The diagonal line is the ground truth. Note again the high accuracy of the bright pixels.

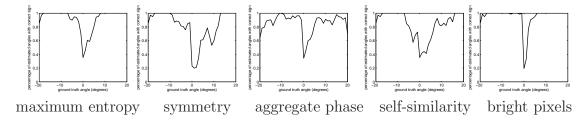


Figure 8.4: Plots of the orientation sign estimates for the five techniques. Each plot shows, for each angle of the robot, the percentage of images across the database in which the technique estimated the sign of the orientation correctly, with the center of the image corresponding to a heading of zero.

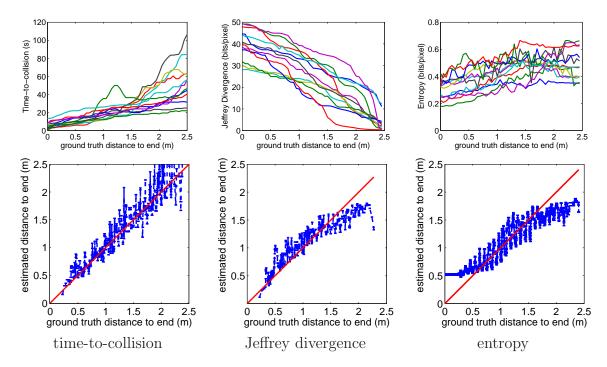


Figure 8.5: ToP: The three measures plotted versus the distance from the robot to the end of the corridor. As the robot approaches the end, the entropy and time-to-collision decrease, while the Jeffrey divergence increases. Each line is a separate run of the robot along a different corridor / location within the corridor. Bottom: Estimated distance to the end of the corridor plotted against ground truth (obtained from the laser) for all three measures. Each vertical error bar indicates $\pm 2\sigma$, where σ is the standard deviation.

from the center), and down the right side (1.5 feet from the center). While driving, the robot collected 640×480 images along with their corresponding 180-degree laser readings. The three measures for estimating the distance to the end were compared with ground truth, which was estimated from the central laser reading after median filtering.

Figure 8.5 shows the results of the three measures. After performing a linear fit to determine the two scale factors α_2 and α_3 , all three measures performed reasonably well at estimating the distance to the end, with time-to-collision being the most accurate. All measures performed more accurately as the robot approached the end of the corridor, until a distance of about 0.25 meters.

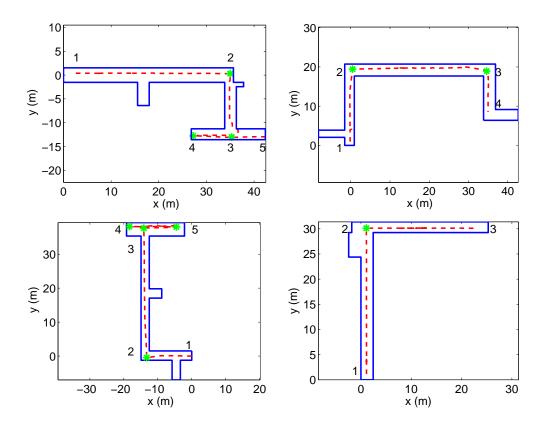
8.3 Exploration in an unknown environment

The completed system consisted of the mobile base with a single forward-facing camera on the front. The only input to the system consisted of the tiny 32×24 downsampled grayscale images from the camera.

The exploration capability of the robot was tested in several corridors. The robot did not have any knowledge of the corridor before the run, and its goal was to autonomously explore the environment by repeatedly driving down the corridor and turning at the end. The turning direction at the end of a corridor was determined by attempting the two possibilities of turning right / turning left in an arbitrary order, using the entropy to distinguish between an open side corridor and a wall. In the event of a dead end, in which case both turning right and turning left are not possible, the robot made a 180-degree turn to return along the direction from which it came.

Results of the system showing successful end-to-end autonomous exploration in several different corridors are displayed in Figure 8.6. The robot was able to stay in the center of the corridor, detect the end, stop, turn 90 degrees in the appropriate direction, and continue driving. The layout of the buildings, along with the path taken by the robot in each run, are shown in the figure. Note that the laser readings were used only to generate the plots, not to guide the robot. We also conducted experiments in which the robot started facing the wall, or started close to a wall; in both cases the robot corrected its orientation and position and continued exploring the environment. The longest successful exploration was a corridor in which the robot continuously ran for 45 minutes, navigating a total (overlapping) distance greater than 850 meters.

A few failure situations are also evident from the plots in the figure. In Riggs-0 and Lowry-0, the final corridor ends in a pair of transparent glass doors or reflective



wall which confuse all the methods for determining the end of the corridor. In Riggs1, the presence of a brightly textured vending machine in the final corridor causes
erroneous estimates for the robot orientation. Note that the robot successfully explores other corridors containing vending machines because the robot has sufficient
time to react, in this corridor the machine is located close to the turn so that it
dominates the robot's field of view immediately after the final left turn. Images from
these environments are shown in Figure 8.7.

In the introduction, we referred to psychological evidence that humans do not need to process image data continuously in order to successfully navigate an environment. And in fact, as a robot moves down a corridor, it is easy to see that consecutive images usually differ from each other by only a small amount. Therefore, we compare the entropy of consecutive images from the current frame t and previous frame t-1,

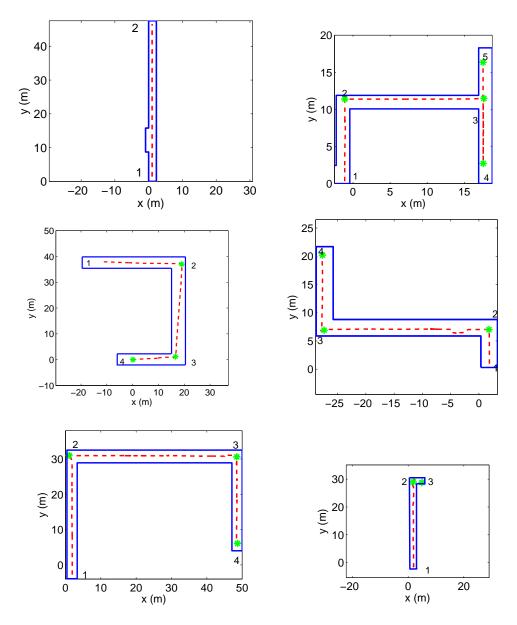


Figure 8.6: Exploration experiments for ten different corridors, showing is the path taken by the robot (red dashed, obtained from laser measurements) and the end-of-corridor detections (green asterisks) along different corridors (blue solid, manually measured). The numbering shows the temporal sequence of the robot's locations from start to end. In lexicographic order, the corridors are Riggs-0, Riggs-1, Riggs-3, Lowry-0,Lowry-2, Freeman-0,Riggs-2, Sirrine-0, Sirrine-2 and Rhodes-4



Figure 8.7: Problematic corridors: (a) reflective glass doors in Riggs-0, (b) reflective wall in Lowry-0, and (c) soda machine in Riggs-1, and (d) glass structures and lack of ceiling lights in EIB-1.

normalized by the first frame of the corridor (which presumably is near the maximum, since the entropy difference decreases as the robot travels down the corridor): $|H(V; I^{(t)}) - H(V; I^{(t-1)})| / H(V; I^{(1)})$. A histogram of these normalized entropy differences is shown in the top of Figure 8.8 for three different corridors, from which it is clear that most differences are small. As a result, our final system processes each image a minimal amount in order to determine whether the image needs to be fully processed by the five methods for orientation and three methods for distance-to-the-end. If the normalized entropy difference is less than 0.01 (10%), then no further processing is performed on the image. The results of this rapid perception are shown in the middle and bottom of the figure, from which it can be seen that nearly 80% of the images are only minimally processed.

8.4 Computational efficiency

To perform the entire processing on a single image (all five measures for estimating the orientation, plus all three measures for estimating the distance to the end), the system takes 3.65 ms. However, the rapid perception module mentioned above quickly determines whether the current image needs to be processed in its entirety. This module requires just 0.28 ms to make that decision, and 80% of the images are

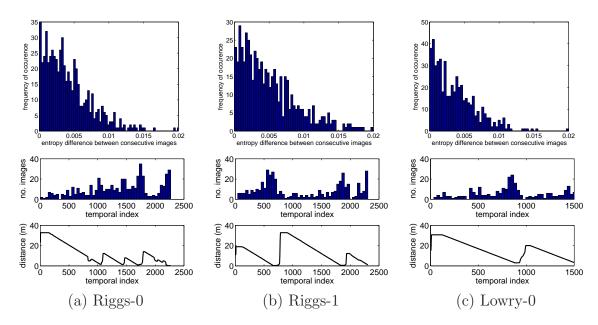


Figure 8.8: Rapid perception for three different corridors. Top: Histogram of normalized entropy difference between consecutive images; most values are less than 0.01. MIDDLE: The number of images fully processed by the system versus the temporal index in the image sequence; most images are discarded after the rapid perception processing. Each bin captures 50 consecutive images, so that complete processing of all frames would be indicated by all bars reaching a height of 50. The percentage of frames fully processed, approximately 20%, is therefore the area under the curve divided by the area of the rectangle of height 50 and length equal to the number of frames in the sequence. Bottom: The distance from the robot to the end of the corridor versus the image index. By comparing the two plots for each corridor, note that when the robot nears the end of the corridor, the number of images fully processed increases.

Image capture and display	$0.04~\mathrm{ms}$
Downsampling	0.18 ms
Maximum Entropy	$0.02 \mathrm{\ ms}$
Maximum Symmetry	0.16 ms
Aggregate Phase	$0.02~\mathrm{ms}$
Vanishing point(self-similarity)	1.5 ms
Median of bright pixels	1.39 ms
Time-to-collision	$0.26~\mathrm{ms}$
Entropy	$0.06~\mathrm{ms}$
Jeffrey divergence	$0.02~\mathrm{ms}$
Total	3.65 ms

Table 8.1: Performance: Time taken by the different vision modules.

not processed further. Therefore, the time needed to process an image frame, on average, is (0.8)(0.28) + (0.2)(3.65) = 0.954 ms, which is equivalent to processing about 1000 frames per second. Stated another way, with a standard 30 Hz camera, the system consumes only 3% of the CPU, thus freeing the processor for other concurrent tasks that might be needed in a real system.

8.5 Corridor junction classification

The robot was mounted with a SICK LMS-291 laser scanner, and a Logitech QuickCam 4000 webcam and made to turn 360° at various types of indoor corridor junctions (dead end, middle, L-junction, T-junction, cross-junction). The image entropy was plotted along with the actual depth readings from the laser scanner. reading every 2 degrees. only used center reading of laser after median filtering. (Sirrine, Lowry, Freeman, Rhodes).

The classification of the corridors using entropy peaks can be analyzed by representing the results in a confusion matrix [42]. A confusion matrix is of size $m \times m$, where there are m labels and shows the percentage of predicted and actual

	p	n	total
p'	True Positive	False Positive	Ρ'
n'	False Negative	True Negative	N'
Total	р	n	

Table 8.2: Table representing the four outcomes of a problem. true positive, true negative, false positive, false negative. These can be used to construct the ROC (receiver operating characteristics) curve.

classifications. Metrics accuracy, true positive rate, true negative rate, precision, false positive rate, false negative rate can be calculated using the confusion matrix as shown in Table 8.5. In signal detection theory, a receiver operating characteristic (ROC), or simply ROC curve, is a graphical plot of the sensitivity, or true positive rate, vs. false positive rate, for a binary classifier system as its discrimination threshold is varied. The ROC can also be represented equivalently by plotting the fraction of false negatives out of the positives (FAR = false acceptance rate) vs. the fraction of true positives out of the negatives (TPR = true positive rate). Also known as a Relative Operating Characteristic curve, because it is a comparison of two operating characteristics (FAR and TPR) as the criterion changes.

$$TPR = \frac{FN}{P} = \frac{TP}{(TP + FN)} \tag{8.1}$$

$$FAR = \frac{FP}{N} = \frac{FP}{(FP + TN)} \tag{8.2}$$

There are two discriminating criteria in the algorithm used for detecting/classifying peaks. One is the Gaussian kernel size used for smoothing k (σ is dependent on k by the following relationship $\sigma = \sqrt{k/2}$. The second parameter is the minimum distance between peaks w. By keeping the k as 80 by trial and error, we plot the ROC curve for varying w to obtain the optimum value. The ERR (Equal error rate) is the

	D	Μ	L	Τ	X
D	3	3	0	1	0
Μ	0	30	0	1	0
L	0	1	3	4	0
Τ	0	2	0	5	0
X	0	0	0	0	1

Table 8.3: Corridor classification

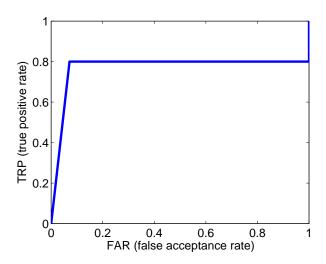


Figure 8.9: ROC curve depicting the success of the classifier. The ERR was found to be 0.14 and the corresponding value of the parameter w was found to be 32.

endtabular

value at which the FAR = (1-TPR) and we can identify the corresponding values of the parameter for that. Its corresponds to the best performance that can be obtained from the classifier. See Figure 8.9.

8.6 Minimalistic corridor representation and reconstruction

For orientation, we collected data for 4 different buildings, 8 unique corridors (1 training + 7 for testing). For every unique corridor, at equally spaced intervals

along the corridor (15 ft), we rotated the robot from $-20^{\circ}to + 20^{\circ}$ and collected corresponding odometry (heading), laser readings (span of $-90^{\circ}to + 90^{\circ}$) and images. We ran the entropy detector, light detector and symmetry detector on the images and compared with ground truth (odometry and/or laser). Since a linear relationship exits between the detected pixel location corresponding to the center of the corridor and the robot orientation as explained in previous sections, we use either the estimate f_l or $(f_h + f_s)/2$.

For wall-floor boundary and corridor reconstruction, we collected data for 11 distinct corridors in 6 different buildings. Drove robot three times (middle, left, right separated by 1.5 feet) along each corridor. and collected images along with their corresponding laser readings $(-90^{\circ}to + 90^{\circ} \text{ sweep})$

The parameters for a linear fit between the location of the orientation line and predicted orientation were estimated by using one of the corridors as a training set. Using the trained parameters, the orientations for all the other data for the remaining 7 test corridors (θ) were predicted from the mean pixel locations using the above equations. The mean error between ground truth (laser) and predicted values of heading was calculated for each of the 7 resolutions considered 320×240 , 160×120 , 80×60 , 64×48 , 32×24 , 16×12 and 8×6 . The results are shown in Figure 8.10.

We show that, with indoor low-resolution images the results of Kong *et al.* [43] are significantly less accurate for determining the wall-floor boundary as well as the orientation line (and therefore the vanishing point). See Figure 8.11 for some examples.

A comparison of our results on four different resolutions is shown in Figure 8.15. It can be seen that the results are consistent across all the four resolutions, 320×240 , 80×60 , 32×24 and 16×12 . This strengthens our argument in favor of using low-resolution information for basic navigation tasks.

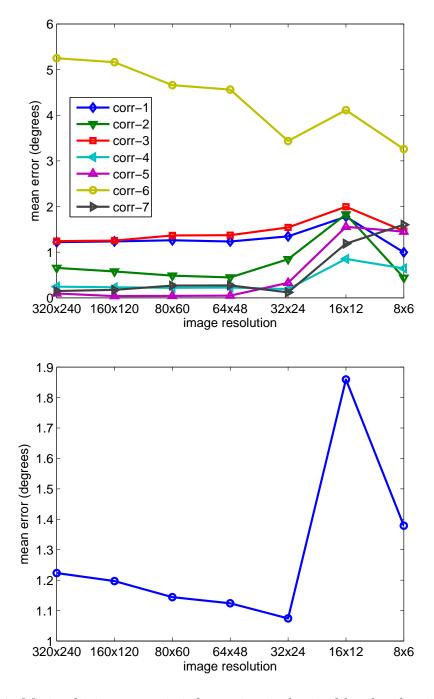


Figure 8.10: Minimalistic geometric information is obtained by the algorithm at very low image resolutions. Top: Mean error (degrees) for each of the 7 test corridors. BOTTOM: Mean error (degrees) of all the 7 test corridors. The orientation estimation error remains relatively stable across different image resolutions. In fact the error drops for a few corridors at 32×24 , primarily due to the fact that downsampling removes artifacts such as reflections and other noise on the walls and floor.

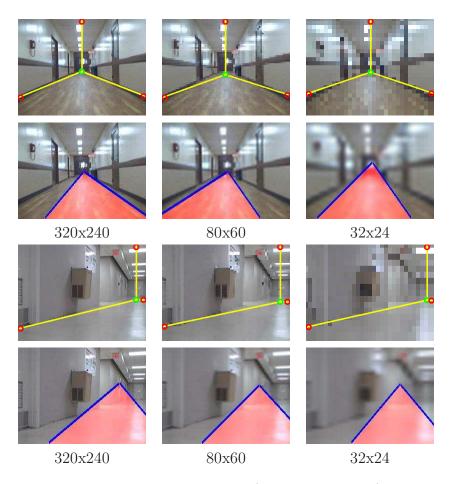


Figure 8.11: Comparison between our results (three yellow lines) and those of Kong $et\ al.\ [43]$ (pink region). Our algorithm achieves more accurate estimation of both the orientation line and the wall-floor boundary in indoor scenes, particularly at low resolutions.

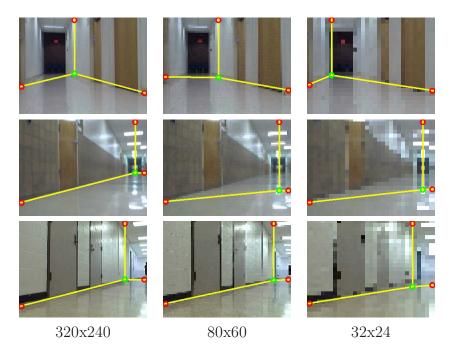
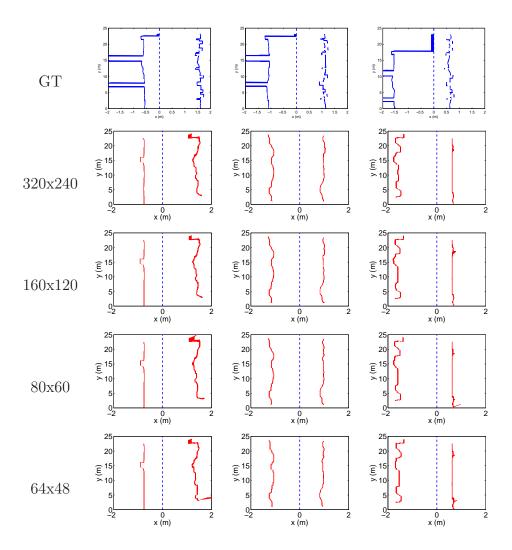


Figure 8.12: Additional results for other corridors, including one without ceiling lights. In some cases, the low-resolution images yield more accurate results.



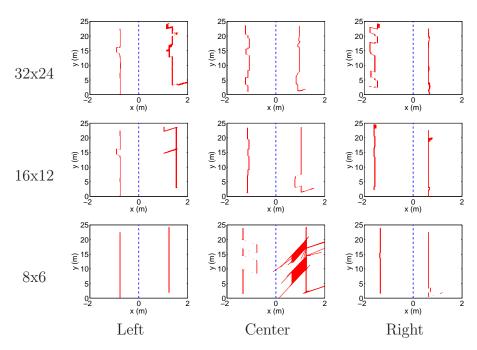


Figure 8.13: Corridor structure reconstruction from the wall-floor boundary, displayed as a top-down view. The topmost row in blue shows the ground truth location of the walls (Cartesian conversion of polar laser readings), and the next 7 rows in red show the reconstruction results from the wall-floor boundaries on different resolution images. Each column represents a different run of the robot in the same corridor, with the robot placed at a different lateral position in the corridor for each run (The position of the robot is shown by the dotted line at 0). Surprisingly, the structure was captured accurately in all resolutions. The error in the results for 86 resolution for the central trial run are spikes that become more pronounced when warped using the floor-image homography.

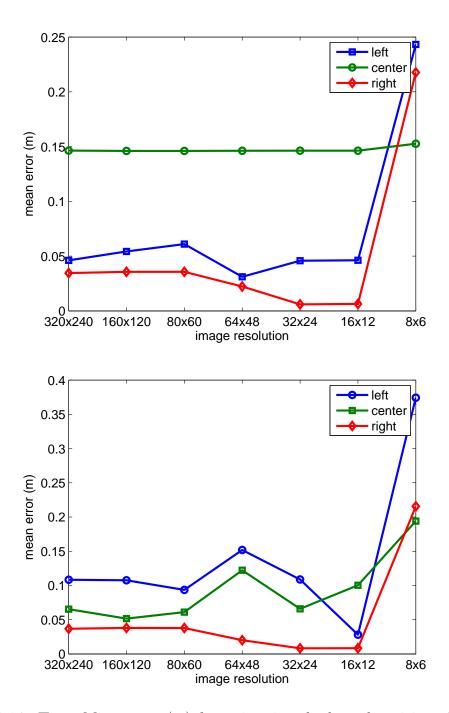


Figure 8.14: Top: Mean error (m) for estimating the lateral position of the robot for three runs in a single corridor. The structure was accurately captured in all three cases. Bottom: Mean error (m) for the estimation of the corridor width. There is not much difference in estimation error rates across the different resolutions, and in fact the error drops in some cases for 32x24 and 16x12 sizes due to the removal of noise and artifacts by downsampling.

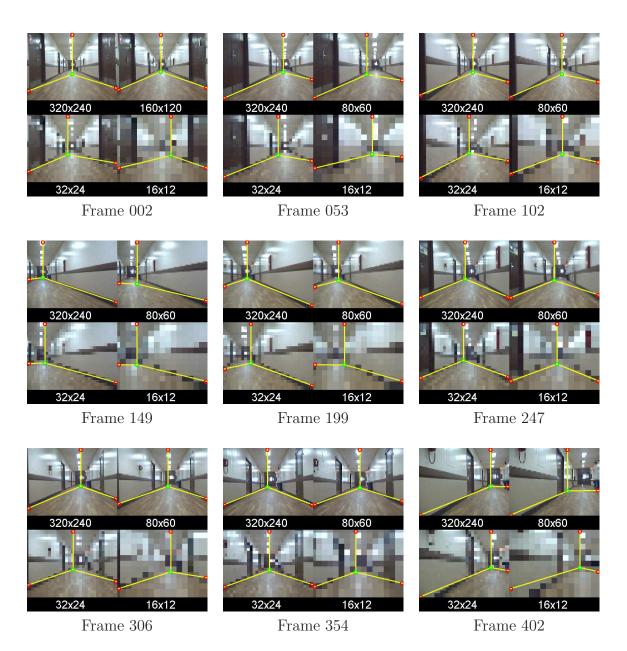


Figure 8.15: Showing four different resolutions (320×240 , 80×60 , 32×24 and 16×12), with minimalistic geometry estimation for corridor sequences. It can be seen that the results show consistent success across varying resolutions and in come cases better results for the lower resolutions.

Chapter 9

Conclusion

The study of low-resolution images plays an important role in the understanding of visual scenes. Interpretation of scenes for primitive tasks can be accomplished using information obtained from images at exceedingly low-resolutions represented by less than 5000 bits at every frame captured. The ability to understand the elementary properties of an image at lower resolutions may be the key to solving a large number of computer vision tasks at increasingly higher orders of speed. Some standard challenges faced by standard computer vision algorithms such as lack of texture and lack of edges are addressed well by low-resolution techniques. Optimization of speed is also achieved as a result of using low-resolution images that is conducive for systems like hand-held devices and micro-embedded devices which are constrained in memory and processor speed due to miniaturization. Furthermore there is evidence to show that certain processes (peripheral vision) occur in low-resolution in humans motivating the need for developing algorithms in computer vision that can successfully work with low-resolution images.

9.1 Contributions

This work represents a collection of some algorithms that work on exceedingly low-resolution images to provide basic information for indoor robot navigation. The main contributions of this dissertation are listed below:

9.1.1 Autonomous exploration

We have presented a low-resolution vision-based robot exploration system that can navigate down the center of a typical unknown indoor corridor, and turn at the end of the corridor. The exploratory behavior of a mobile robot is modeled by a set of visual percepts that work in conjunction to correct its path in an indoor environment based on different measures. Special emphasis is placed on using low-resolution images for computational efficiency, and on measures that capture information content that cannot be represented using traditional point features and methods. The resultant algorithm enables end-to-end navigation in indoor environments with self-directed decision making at corridor ends, without the use of any prior information or map. The primary contribution of this work is the spatio-temporal compression of image information that is needed for computing navigation parameters of the robot, yielding a high computational efficiency while maintaining robustness.

We throw away 99.75% of spatial information (downsampling) and 80% of temporal information (rapid perception), leading to an algorithm that works on just 0.02% of the information available. The advantage of such information reduction is not only the tremendous computational efficiency which frees processor cycles to perform higher-level tasks such as recognition, but also the proof-of-concept regarding the amount of information needed for a particular task, in the spirit of minimalistic sensing.

9.1.2 Junction classification

We have presented a classification of junction types for indoor environments using information theory. Our approach showed a correlation between image entropy and corridor depth. We show a classifier that it built using entropy values measured as a robot turns at corridor junctions that classifies five different junction types (dead-end, middle, T-junction, L-junction, X-junction) with reasonable accuracy. We extend the concept to unwrapped omnidirectional images and we show that the same algorithm can be used to detect and classify corridors in such images with the added advantage that only a single image is needed at each junction for such a classification. The proposed algorithm was tested on images from several corridors showing the feasibility of using entropy for detecting open corridors.

9.1.3 Minimalistic corridor representation

We have proposed an algorithm to extract a minimalistic geometric representation of a typical indoor corridor environment using low resolution images. Motivated by the "selective degradation hypothesis," our approach exploits the redundancy of image information in order to extract useful information for mobile robotic tasks with minimal processing. Our algorithm combines two ideas: extracting the wallfloor boundary by combining intensity edges and specular reflection removal, and centerline estimation using a combination of information theoretic cues and bright pixel estimation. Previous approaches for these problems have been extended and modified to facilitate low resolution processing.

The proposed algorithm was tested on images from several different corridors, showing that the accuracy of the estimation of the orientation line or corridor geometry changed very little even when more than 99% of the original information was

discarded by downsampling the image to an extremely low resolution. Our approach can be seen as an exploration into identifying how much information is needed for basic mobile robot tasks such as corridor exploration and navigation. By reducing the resolution required for these basic tasks, the CPU time is freed for other tasks that potentially require higher resolutions and more involved processing.

9.2 Future work

One of the major outcomes of our research endeavor is the presentation of a set of techniques using information theory to identify the optimal resolution needed for robot exploration. The same technique can be used to develop a general methodology for several such applications and new problems in computer vision. Information theory can be used to determine the amount of information needed to perform a specific tasks. Some examples include determining the resolution for automatic target recognition (ATR) and the resolution needed for video transmission.

There is much room for improvement in this line of work. First, all the algorithms are challenged by specular or transparent surfaces, particularly when they dominate the field of view. However, this limitation does not seem to be intrinsic to the reduced amount of information, since a human viewer has no trouble interpreting the low-resolution information. This leads to the question of exploring atypical corridors and environments in which the algorithm currently fails. A potential task could be to tailor the information theoretic measures combined with other measures to achieve autonomous exploration in different indoor structures like atriums, court-yards, lounges, office spaces, labs, and rooms in general, where the general structure of the corridor could change from being long and rectangular to a square room, curved structures, corridors, and so on. Apart from exploration such indoor environments

would also require some sort of dynamic obstacle avoidance. One suggestion would be the use of relative entropy and crude optical flow techniques to detect and avoid obstacles.

Another improvement would be to combine the low-level exploration capabilities of such a robot with high-level recognition algorithms to provide a more detailed sense of the robot's location within the environment by recognizing landmarks. Ultimately, we believe that minimalistic low-resolution sensing is a promising approach for low-level mobile robot tasks such as navigation and exploration.

We intend to explore the concept of self-similarity for vanishing points over different scales and study the effect of scale both spatially and temporally for robot exploration tasks. Experiments performed with even lower spatial resolutions of 16×12 and 8×6 will help establish the spatial limit for different measures. Other future work may involve achieving localization by combining this exploration technique with existing vision based SLAM algorithms. The ultimate goal is to achieve local-global localization by an autonomous navigating robot in an environment-independent manner with strong emphasis on low-resolution and simplicity of the algorithms used.

Appendices

Appendix A

Time-to-contact Relative to a

Planar Surface

Horn et al. [29] have described the calculation of time-to-contact using spatial and temporal image derivatives and can be computed using just two frames in a sequence. The system does not use any tracking or calibration. The camera is assumed to be moving perpendicular to a planar surface.

If the distance from the approaching surface is Z, then the time-to-contact is defined as

$$T = \frac{-Z}{\frac{dZ}{dt}}$$

where $\frac{dZ}{dt}$ is the derivative of the distance with respect to time. According to perspective projection equations, if S is the length of the cross-section of the approaching planar object and s is the size of its image, then, $\frac{s}{f} = \frac{S}{Z}$ where f is the focal length of the camera, which implies that $S\frac{dZ}{dt} + Z\frac{ds}{dt} = 0$ (see Figure A.1).

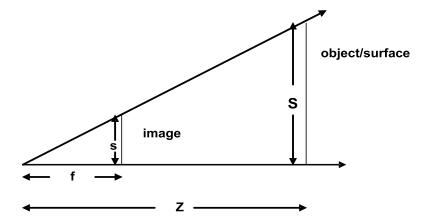


Figure A.1: Perspective projection.

Then $S\frac{dZ}{dt} = -Z\frac{ds}{dt}$ which implies that

$$\frac{-Z}{\frac{dZ}{dt}} = \tau_{TTC} = \frac{S}{\frac{ds}{dt}} \tag{A.1}$$

Considering the brightness constancy assumption of an image E, (the brightness of a pixel corresponding to a point on the object does not change with time), we have

$$E(x + \Delta x, y + \Delta y, t + \Delta t) = E(x, y, t)$$

Assuming small motion between successive frames (small Δx and Δy), the above can be expanded using first order Taylor's series to get

$$E_x \frac{dx}{dt} + E_y \frac{dy}{dt} + E_t = 0$$

or

$$uE_x + vE_y + E_t = 0 (A.2)$$

where $u=\frac{dx}{dt}$ and $v=\frac{dy}{dt}$ respectively, $E_x=\frac{\partial E}{\partial x}$ and $E_y=\frac{\partial E}{\partial y}$ are spatial image

brightness derivatives and $E_t = \frac{\partial E}{\partial t}$ is the temporal brightness derivative.

Once again obtaining perspective projection equations of the camera

$$\frac{x}{f} = \frac{X}{Z}$$
 and $\frac{y}{f} = \frac{Y}{Z}$ (A.3)

where X, Y, and Z are coordinates of a point in space and x, y are corresponding image coordinates. Differentiating equation (A.3) with respect to time, we get

$$\frac{u}{f} = \frac{U}{Z} - \frac{X}{Z} \frac{W}{Z}$$
 and $\frac{v}{f} = \frac{V}{Z} - \frac{Y}{Z} \frac{V}{Z}$ (A.4)

where U, V, W are temporal derivatives of X, Y, Z respectively and represent velocity of the point on the object relative to the camera. u, v are temporal derivatives of x and y (the motion field in the image). Substituting equation (A.3) in equation (A.4), we get

$$\frac{u}{f} = \frac{U}{Z} - \frac{x}{f} \frac{W}{Z}, \quad \text{and} \quad \frac{v}{f} = \frac{V}{Z} - \frac{y}{f} \frac{V}{Z}$$
 (A.5)

which leads to

$$u = \frac{1}{Z}(fU - xW)$$
 and $v = \frac{1}{Z}(fV - yW)$ (A.6)

Considering the simple case where the translation is perpendicular to the optical axis (see Figure A.2), U and V can be set to 0 in equation (A.6).

$$u = -x\frac{W}{Z}$$
 and $v = -y\frac{V}{Z}$ (A.7)

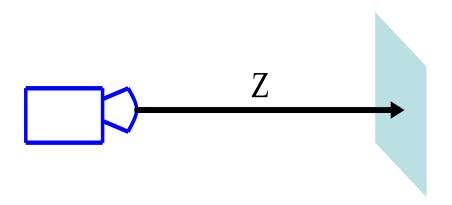


Figure A.2: Camera moving such that optical axis is perpendicular to the approaching surface.

Substituting equation (A.7) in equation (A.2), we get

$$-\frac{W}{Z}(xE_x + yE_y) + E_t = 0 \tag{A.8}$$

or

$$CG + E_t = 0 (A.9)$$

where $C = -\frac{W}{Z}$ from equation (A.1) and is the inverse of TTC, and $G = xE_x + yE_y$.

Formulating a least squares method to minimize $\sum (CG + E_t)^2$ where the sum is over all pixels of interest, which could be the whole image, we get

$$\sum (CG + E_t) G = 0$$

$$C = \frac{\sum G(x,y) E_t}{-\sum (G(x,y))^2}$$
(A.10)

It is evident that when C increases, TTC decreases. Intuitively this explains that as the camera approaches the surface being viewed, the temporal change in brightness values increases rapidly and the spatial change decreases (because when

the object/surface grows bigger, the sum of spatial gradients is lower), and therefore the TTC decreases as the object/surface looms closer to the camera.

Appendix B

Kalman Filter

If we consider a process of a system described by a linear model, in discrete time, we can describe the process state, the input, the measurements and the measurement and process noise. The Kalman filter is a powerful state estimation technique that can then be used to estimate the state (unknown) of the system by using a sequence of measurements and the input. The Kalman filter can produce true values of measurements by predicting a state value, while estimating the uncertainty of the predicted value, and computing a weighted average of the predicted value and the measured value where the weights are associated with the noise covariances in the measurements and the process [28]. For the success of a Kalman filter there are two important assumptions. One is that the process has a linear model. The other is that the noise (measurement and process) have a normal distribution. According to the descriptions of Bishop and Welch [99], the equations of the Kalman filter fall into two groups: time update equations and measurement update equations. The time update equations are responsible for incorporating a new measurement into the a priori estimate to obtain an improved a posteriori estimate. The time update equations can be described as predictor equations, and the measurement update equations as corrector equations.

B.1 Kalman filter, matrix notation

This section is described from class notes [28]. We show here for illustration, a two variable state (position and velocity). We will now proceed to show the setting up of the Kalman filter essentials in matrix form that will make is easier to set up the equations. The measurements can be represented as follows (we assume a linear relationship between the state and the measurements).

$$Y_t = MX_t + N_t \tag{B.1}$$

where Y_t is the measurements, X_t is the actual state of system (position and velocity) at time t, M is the observation matrix (the part of system that is observable and this constitutes measurements from different sensing modalities in general) and N_t Random noise during sensing. In this illustration, only the position was measured at each instance of time.

$$[y_t] = \begin{bmatrix} 1 & 0 \end{bmatrix} \begin{bmatrix} x_t \\ \dot{x}_t \end{bmatrix} + [n_t]$$
 (B.2)

Similarly, the state transition can be written as

$$X_{t+1} = \Phi X_t + U_t \tag{B.3}$$

where U_t represents the random dynamics between t and t+1, X_{t+1} the actual state of system at time t+1 and Φ is the state transition matrix. We are assuming a

constant velocity model here. The detailed equation is re-written as

$$\begin{bmatrix} x_{t+1} \\ \dot{x_{t+1}} \end{bmatrix} = \begin{bmatrix} 1 & T \\ 0 & 1 \end{bmatrix} \begin{bmatrix} x_t \\ \dot{x}_t \end{bmatrix} + \begin{bmatrix} 0 \\ u_t \end{bmatrix}$$
(B.4)

where u_t is the random acceleration during t...t+1. For simplicity, the dynamic noise during T, is assumed to be zero. This leads us to,

$$X_{t+1} = \Phi X_t \tag{B.5}$$

The filtering equation can be written as

$$X_{t,t} = X_{t,t-1} + K_t(Y_t - MX_{t,t-1})$$
(B.6)

where $X_{t,t-1}$ is the predicted state from previous measurements, $X_{t,t}$ is the Kalman filtered state from two estimates, K_t is the Kalman gain matrix (weighting of estimates). The Kalman gain is calculated at every time step as follows

$$K_t = S_{t,t-1} + M^T \left[R_t + M S_{t,t-t} M^T \right]^{-1}$$
(B.7)

where $S_{t,t-1}$ is the predicted covariance from previous estimates and R_t observation noise covariance. An estimate of our accuracy at prediction is also calculated at each step. The prediction can be written as

$$S_{t+1,t} = \Phi S_{t,t} \Phi^T + Q_t \tag{B.8}$$

where Q_t dynamic noise covariance. The update of the covariance can be written as:

$$S_{t,t} = [I - K_t M] S_{t,t-1}$$
(B.9)

where I identity matrix.

B.2 Kalman filter in operation

The Kalman filter algorithm works in a loop with predict/update calculations at eat time-step. We start by assuming in most cases that the state is unknown. In this illustration, we assume zero position and velocity. The initial prediction is also assumed to be zero (or unknown).

$$X_{0,0} = 0X_{1,0} = 0 (B.10)$$

The measurement noise covariance matrix is known. The measurement noise can be obtained in various ways by observing the measurements for a specific position over a period of time. Assuming a constant velocity model, we have

$$R = [\sigma^2] \tag{B.11}$$

The dynamic noise covariance matrix is

$$Q = \begin{bmatrix} 0 & 0 \\ 0 & \sigma_u^2 \end{bmatrix} \tag{B.12}$$

where σ_u is the dynamic state noise and described the random acceleration in the system. This is in general very difficult to measure and is obtained by tuning the

Kalman filter once the other constants are established.

We initialize S, the accuracy of the predictions to the dynamic covariance Q for simplicity.

$$S_{0,0} = S_{1,0} = Q \tag{B.13}$$

The following steps are repeated in a loop for Kalman filter operation and at the end of each loop t is incremented.

$$K_t = S_{t,t-1} M^T [MS_{t,t-1} M^T + R]^{-1}$$
(B.14)

$$X_{t,t} = X_{t,t-1} + K_t[Y_t - MX_{t,t-1}]$$
(B.15)

$$S_{t,t} = [I - K_t M] S_{t,t-1}$$
 (B.16)

$$X_{t+1,t} = \Phi X_{t,t} S_{t+1,1} = \Phi X_{t,t} S_{t,t} \Phi^T + Q_t$$
(B.17)

Appendix C

Visual Detection of Light Sources

In a classic paper Ullman [95] describes six factors that are associated with the detection of light sources in an image and therefore can be used to differentiate it from the specular reflections. This is of enormous importance in indoor environments where reflections occur far too often.

- The highest intensity in the visual field: Ullman states that having the highest intensity in the scene is neither a necessary nor a sufficient condition for a light source. Reflections and light sources often have the same intensities.
- High absolute intensity value: Pixels associated with a light source need not
 have high absolute intensity. There are examples of dim lamps viewed against
 a dark background as an example.
- Local contrast: Local contrast is an important and differentiating factor to be considered for evaluating a point as a light source. The contrast between intensity I_1 and intensity I_2 can be defined as $\frac{I_1-I_2}{I_1+I_2}$, according to Ullman. This happens to be a monotonic function of $\frac{I_1}{I_2}$ indicating how many timed a pixel is brighter than another (neighboring pixel).

- Global contrast: Contrast when applied globally in the image compares the brightest and the darkest intensities in the image.
- Intensity compared with the average intensity in the scene: Another factor that has been considered is the influence of changes in average illumination. It was deemed by Ullman that it does not affect the detection rate of light sources.
- Lightness computation: Lightness can be used to differentiate between sharp intensity changes and the gradual intensity changes. In other words intensity gradient along a certain direction can be used to determine the presence of a light source. Sharp intensity changes signify the presence of a light source.

It can be seen from the discussion of the factors that the only two factors which play a role in determining the light sources are 'contrast' and 'lightness'.

Bibliography

- [1] N. Ancona and T. Poggio. Optical flow from 1-D correlation: Application to a simple time-to-crash detector. *International Journal of Computer Vision*, 14(2):131–146, Mar. 1995.
- [2] J. Andre, D. A. Owens, and L. O. Harvey, Jr., editors. *Visual perception : The influence of H. W. Leibowitz*. Washington, DC: American Psychological Association, 2003.
- [3] M. Atallah. On symmetry detection. In IEEE Transactions on Computers, 34('7):663-666, 1985.
- [4] A. Basu and X. Li. A framework for variable-resolution vision. In *Proceedings* of the International Conference on Computing and Information: Advances in Computing and Information, pages 721–732, 1991.
- [5] H. Bay, A. Ess, T. Tuytelaars, and L. V. Gool. SURF: Speeded up robust features. *Computer Vision and Image Understanding*, 110(3):346–359, June 2008.
- [6] H. Bay, T. Tuytelaars, and L. V. Gool. SURF: Speeded up robust features. In 9th European Conference on Computer Vision, Graz Austria, May 2006.
- [7] E. Bayramoglu, N. Andersen, N. Kjolstad Poulsen, J. Andersen, and O. Ravn. Mobile robot navigation in a corridor using visual odometry. In *International Conference on Advanced Robotics*, pages 1 –6, June 2009.
- [8] G. Blanc, Y. Mezouar, and P. Martinet. Indoor navigation of a wheeled mobile robot along visual routes. In *Proceedings of the IEEE International Conference on Robotics and Automation (ICRA)*, pages 3354–3359, 2005.
- [9] J.-L. Blanco, J.-A. Fernández-Madrigal, and J. Gonzalez. A new approach for large-scale localization and mapping: Hybrid metric-topological SLAM. In *Proceedings of the International Conference on Robotics and Automation*, 2007.
- [10] B. Bonev, M. Cazorla, and F. Escolano. Robot navigation behaviors based on omnidirectional vision and information theory. *Journal of Physical Agents*, 1(1):27–35, September 2007.

- [11] J. C. Brooks and D. A. Owens. Effects of luminance, blur, and tunnel vision on postural stability. *Journal of Vision*, 1(3):304, 2001.
- [12] J. M. Buhmann, W. Burgard, A. B. Cremers, D. Fox, T. Hofmann, F. E. Schneider, J. Strikos, and S. Thrun. The mobile robot RHINO. AI Magazine, 16(2):31–38, 1995.
- [13] Z. Chen and S. T. Birchfield. Qualitative vision-based mobile robot navigation. In *Proceedings of the IEEE International Conference on Robotics and Automation (ICRA)*, pages 2686–2692, May 2006.
- [14] M. Cho and K. Lee. Bilateral symmetry detection via symmetry-growing. In In the Proceedings of the British Machine Vision Conference, pages 1–8, 2009.
- [15] K. Choi, S. Bae, Y. Lee, and C. Park. A lateral position and orientation estimating algorithm for the navigation of the vision-based wheeled mobile robot in a corridor. In *SICE 2003 Annual Conference*, volume 3, 2003.
- [16] Y.-H. Choi, T.-K. Lee, and S.-Y. Oh. A line feature based SLAM with low grade range sensors using geometric constraints and active exploration for mobile robot. *Autonomous Robots*, 24(1):13–27, January 2008.
- [17] D. Coombs, M. Herman, T. Hong, and M. Nashman. Real-time obstacle avoidance using central flow divergence and peripheral flow. *IEEE Transactions on Robotics and Automation*, 14(1):49–59, Feb 1998.
- [18] A. J. Davison and N. Kita. 3D simultaneous localisation and map-building using active vision for a robot moving on undulating terrain. In *Proceedings* of the IEEE Conference on Computer Vision and Pattern Recognition, pages 384–391, 2001.
- [19] A. J. Davison and N. Kita. Sequential localization and map-building for real-time computer vision and robotics. *Robotics and Autonomous Systems*, 36(4):171–183, 2001.
- [20] A. J. Davison and D. W. Murray. Simultaneous localization and map-building using active vision. *IEEE Transactions on Pattern Analysis and Machine In*telligence, 24(7):865–880, July 2002.
- [21] A. J. Davison, I. D. Reid, N. D. Molton, and O. Stasse. MonoSLAM: Real-time single camera slam. *IEEE Transactions on Pattern Analysis and Machine Intelligence*, 29(6):1052–1067, June 2007.
- [22] G. N. DeSouza and A. C. Kak. Vision for mobile robot navigation: A survey. *IEEE Transactions on Pattern Analysis and Machine Intelligence*, 24(2):237–267, 2002.

- [23] F. Escolano, B. Bonev, P. Suau, W. Aguilar, Y. Frauel, J. Saez, and M. Cazorla. Contextual visual localization: cascaded submap classification, optimized saliency detection, and fast view matching. In *IEEE International Conference on Intelligent Robots and Systems*, 2007.
- [24] S. Han, G. W. Humphreys, and L. Chen. Uniform connectedness and classical gestalt principles of perceptual grouping. *Perception & Psychophysics*, 61(4):661–674, 1999.
- [25] C. G. Harris and M. Stephens. A combined corner and edge detector. In *Proceedings of the 4th Alvey Vision Conference*, pages 147–151, 1988.
- [26] S. Hayashi and O. Hasegawa. Detecting faces from low-resolution images. In *Proceedings of the 7th Asian Conference on Computer Vision*, pages 787–796, 2006.
- [27] H. Hirschmüller. Stereo processing by semi-global matching and mutual information. *IEEE Transactions on Pattern Analysis and Machine Intelligence*, 30(2):328–341, Feb. 2008.
- [28] A. Hoover, 2006. Class Notes in Analysis of Robotic Systems.
- [29] B. K. P. Horn, Y. Fang, and I. Masaki. Time to contact relative to a planar surface. *IEEE Intelligent Vehicles Symposium*, pages 68–74, June 2007.
- [30] I. Horswill. Specialization of perceptual processes. Technical Report AITR-1511, MIT-AI, 1994.
- [31] I. D. Horswill. Polly: A vision-based artificial agent. In *Proceedings of the National Conference on Artificial Intelligence*, pages 824–829, 1993.
- [32] G. M. Jenkins and D. G. Watts. *Spectral Analysis and its applications*. Holden-Day, 1968.
- [33] S. D. Jones, C. S. Andersen, and J. L. Crowley. Appearance based processes for visual navigation. In *Proceedings of the IEEE/RSJ International Conference* on *Intelligent Robots and Systems (IROS)*, pages 551–557, 1997.
- [34] T. Judd, F. Durand, and A. Torralba. Fixations on low-resolution images. Journal of Vision, 11(4):1–20, 2011.
- [35] A. A. Kalia, G. E. Legge, and N. A. Giudice. Learning building layouts with non-geometric visual information: The effects of visual impairment and ages. *Perception*, 37(11):1677–1699, Nov 2008.
- [36] K. Kanatani. Symmetry as a continuous feature. *IEEE Transactions on Pattern Analysis and Machine Intelligence*, 19(3):246–247, Mar. 1997.

- [37] N. Karlsson, E. D. Bernard, J. Ostrowski, L. Goncalves, P. Pirjanian, and M. E. Munich. The vSLAM algorithm for robust localization and mapping. In Proceedings of the IEEE International Conference on Robotics and Automation (ICRA), pages 24–29, 2005.
- [38] J. Kim, V. Kolmogorov, and R. Zabih. Visual correspondence using energy minimization and mutual information. In *Proceedings of the International Conference on Computer Vision*, 2003.
- [39] J. Klippenstein and H. Zhang. Quantitative evaluation of feature extractors for visual SLAM. In *CRV '07: Proceedings of the Fourth Canadian Conference on Computer and Robot Vision*, pages 157–164, Washington, DC, USA, 2007. IEEE Computer Society.
- [40] J. J. Koenderink. The structure of images. *Biological Cybernetics*, V50(5):363–370, 1984.
- [41] H. Kogan, R. Maurer, and R. Keshet. Vanishing points estimation by self-similarity. In *Proceedings of the IEEE Conference on Computer Vision and Pattern Recognition*, pages 755–761, 2009.
- [42] R. Kohavi and F. Provost. Glossary of Terms. Machine Learning, 30(2-3):271–274, 1998.
- [43] H. Kong, J. Y. Audibert, and J. Ponce. General road detection from a single image. In *IEEE Conference on Computer Vision and Pattern Recognition*, 2009.
- [44] H. Kong, J.-Y. Audibert, and J. Ponce. General road detection from a single image. *IEEE Transactions on Image Processing*, 19(8):2211 2220, Aug. 2010.
- [45] A. Kosaka and A. C. Kak. Fast vision-guided mobile robot navigation using model-based reasoning and prediction of uncertainties. *CVGIP: Image Understanding*, 56(3):271–329, Nov. 1992.
- [46] P. Kovesi. Symmetry and asymmetry from local phase. In *Tenth Australian Joint Conference on Artificial Intelligence*, pages 185–190, Dec. 1997.
- [47] M. F. Land and B. W. Tatler. Steering with the head: The visual strategy of a racing driver. *Current Biology*, 11(15):1215 1220, 2001.
- [48] H. W. Leibowitz, C. S. Rodemer, and J. Dichgans. The independence of dynamic spatial orientation from luminance and refractive error. *Perception & Psychophysics*, 25(2):75–79, Feb. 1979.
- [49] Y. Li and S. T. Birchfield. Image-based segmentation of indoor corridor floors for a mobile robot. In *Proceedings of the IEEE Conference on Intelligent Robots and Systems (IROS)*, Oct. 2010.

- [50] T. Lindeberg. Scale-space theory: A basic tool for analysing structures at different scales. *Journal of Applied Statistics*, 21(2):224–270, 1994.
- [51] L. M. Lorigo, R. A. Brooks, and W. E. L. Grimson. Visually-guided obstacle avoidance in unstructured environments. In *IEEE Conference on Intelligent Robots and Systems*, volume 1, pages 373–379, Sept. 1997.
- [52] D. G. Lowe. Distinctive image features from scale-invariant keypoints. *International Journal of Computer Vision*, 60(2):91–110, 2004.
- [53] J. MacQueen. Some methods for classification and analysis of multivariate observations. In *Proceedings of the 5th Berkeley Symposium on Mathematical Statistics and Probability*, pages 281–297, 1967.
- [54] G. Marola. On the detection of the axes of symmetry of symmetric and almost symmetric planar images. *IEEE Transactions on Pattern Analysis and Machine Intelligence*, 11(1):104–108, January 1989.
- [55] Y. Matsumoto, K. Ikeda, M. Inaba, and H. Inoue. Exploration and navigation in corridor environment based on omni-view sequence. In *Proceedings of the International Conference on Intelligent Robots and Systems*, volume 2, pages 1505–1510, 2000.
- [56] Y. Matsumoto, M. Inaba, and H. Inoue. Visual navigation using view-sequenced route representation. In *Proceedings of the IEEE International Conference on Robotics and Automation (ICRA)*, volume 1, pages 83–88, 1996.
- [57] Y. Matsumoto, K. Sakai, M. Inaba, and H. Inoue. View-based approach to robot navigation. In *Proceedings of the International Conference on Intelligent Robots and Systems*, pages 545–550, 2000.
- [58] G. McLean and D. Kotturi. Vanishing point detection by line clustering. IEEE Transactions on Pattern Analysis and Machine Intelligence, 17(11):1090–1095, 1995.
- [59] M. Meng and A. Kak. NEURO-NAV: A neural network based architecture for vision-guided mobile robot navigation using non-metrical models of the environment. In *Proceedings of the IEEE International Conference on Robotics and Automation*, volume 2, pages 750–757, 1993.
- [60] K. Mikolajczyk and C. Schmid. A performance evaluation of local descriptors. IEEE Transactions on Pattern Analysis and Machine Intelligence, 27(10):1615–1630, Oct 2005.
- [61] M. Milford and G. Wyeth. Persistent navigation and mapping using a biologically inspired SLAM system. *The International Journal of Robotics Research*, 29(9):1131–1153, Aug. 2010.

- [62] M. Montemerlo, S. Thrun, D. Koller, and B. Wegbreit. FastSLAM: A factored solution to the simultaneous localization and mapping problem. In *Proceedings* of the AAAI National Conference on Artificial Intelligence, 2002.
- [63] H. Moravec. Locomotion, vision and intelligence. In M. Brady and R. Paul, editors, *Robotics Research: The First International Symposium*, pages 215–244. Cambridge, Massachusetts: The MIT Press, Aug. 1984.
- [64] V. N. Murali and S. T. Birchfield. Autonomous navigation and mapping using monocular low-resolution grayscale vision. In Workshop on Visual Localization for Mobile Platforms (in association with CVPR), June 2008.
- [65] V. N. Murali and S. T. Birchfield. Autonomous exploration using rapid perception of low-resolution image information (under review). *Autonomous Robots* (*Under Review*), 2011(submitted).
- [66] R. C. Nelson and J. Aloimonos. Using flow field divergence for obstacle avoidance towards qualitative vision. In *Proceedings of the 2nd International Con*ference on Computer Vision, pages 188–196, 1988.
- [67] V. Nguyen, A. Harati, A. Martinelli, R. Siegwart, and N. Tomatis. Orthogonal SLAM: a step toward lightweight indoor autonomous navigation. In *IEEE/RSJ* International Conference on Intelligent Robots and Systems, pages 5007 –5012, oct. 2006.
- [68] J. M. O'Kane and S. M. LaValle. Almost-sensorless localization. In Proc. IEEE International Conference on Robotics and Automation, 2005.
- [69] D. A. Owens. Twilight vision and road safety. In J. Andre, D. A. Owens, and L. O. Harvey, Jr., editors, Visual perception: The influence of H. W. Leibowitz. Washington, DC: American Psychological Association, 2003.
- [70] D. A. Pomerleau. Efficient training of artificial neural networks for autonomous navigation. *Neural Computation*, 3(1):88–97, 1991.
- [71] L. Quan and R. Mohr. Determining perspective structures using hierarchical hough transform. *Pattern Recognition Letters*, 9(4):279–286, May 1989.
- [72] F. T. Ramos, J. I. Nieto, and H. F. Durrant-Whyte. Recognising and modelling landmarks to close loops in outdoor SLAM. In *In Proceedings IEEE International Conference on Robotics and Automation (ICRA)*, pages 2036–2041, Apr. 2007.
- [73] A. Ranganathan, E. Menegatti, and F. Dellaert. Bayesian inference in the space of topological maps. *IEEE Transactions on Robotics*, pages 92–107, 2006.

- [74] E. Rosten and T. Drummond. Fusing points and lines for high performance tracking. In *IEEE International Conference on Computer Vision*, volume 2, pages 1508–1511, October 2005.
- [75] E. Rosten and T. Drummond. Machine learning for high-speed corner detection. In *European Conference on Computer Vision*, volume 1, pages 430–443, May 2006.
- [76] D. B. Russakoff, C. Tomasi, T. Rohlfing, and C. R. Maurer. Image similarity using mutual information of regions. In 8th European Conference on Computer Vision (ECCV), pages 596–607. Springer, 2004.
- [77] G. E. Schneider. Two visual systems. Science, 163(3870):895–902, Feb. 1969.
- [78] S. Se, D. Lowe, and J. Little. Vision-based mobile robot localization and mapping using scale-invariant features. In *Proceedings of the IEEE International Conference on Robotics and Automation (ICRA)*, volume 2, 2001.
- [79] S. Se, D. Lowe, and J. J. Little. Vision-based global localization and mapping for mobile robots. *IEEE Transactions on Robotics*, pages 364–375, 2005.
- [80] S. Segvic and S. Ribaric. Determining the absolute orientation in a corridor using projective geometry and active vision. *IEEE Transactions on Industrial Electronics*, 48(3):696 –710, June 2001.
- [81] S. Shah and J. K. Aggarwal. Mobile robot navigation and scene modeling using stereo fish-eye lens system. *Machine Vision and Applications*, 10(4):159–173, 1997.
- [82] C. E. Shannon. A mathematical theory of communication. *Bell System Technical Journal*, 27:379–423,623–656, 1948.
- [83] D. Shen, H. Ip, K. Cheung, and E. Teoh. Symmetry detection by generalized complex (GC) moments: A close-form solution. *IEEE Transactions on Pattern* Analysis and Machine Intelligence, 21(5):466–476, May 1999.
- [84] J. Shi and C. Tomasi. Good features to track. In *Proceedings of the IEEE Conference on Computer Vision and Pattern Recognition*, pages 593–600, 1994.
- [85] F. Stentiford. Attention-based vanishing point detection. In *Proceedings of the IEEE International Conference on Image Processing*, pages 417–420, 2006.
- [86] C. Sun. Symmetry detection using gradient information. *Pattern Recognition Letters*, 16(9):987–996, September 1995.
- [87] Team ARobAS. Advanced robotics and autonomous systems: 2007 Activity Report. Technical Report RA2007, INRIA, 2007.

- [88] C. Thorpe, M. H. Hebert, T. Kanade, and S. A. Shafer. Vision and navigation for the Carnegie-Mellon NAVLAB. *IEEE Transactions on Pattern Analysis and Machine Intelligence*, 10(3):362–372, May 1988.
- [89] S. Thrun. Robotic mapping: A survey. In G. Lakemeyer and B. Nebel, editors, *Exploring Artificial Intelligence in the New Millenium*. Morgan Kaufmann, 2002.
- [90] A. Torralba. How many pixels make an image? Visual Neuroscience, 26(01):123–131, 2009.
- [91] A. Torralba, R. Fergus, and W. T. Freeman. 80 million tiny images: A large data set for nonparametric object and scene recognition. *IEEE Transactions* on Pattern Analysis and Machine Intelligence, 30(11):1958 –1970, Nov. 2008.
- [92] A. Torralba and P. Sinha. Detecting faces in impoverished images. A.I. Memo 2001-28, MIT-AI, May 2001.
- [93] B. Tovar, L. Guilamo, and S. M. Lavalle. Gap navigation trees: Minimal representation for visibility-based tasks. In *In Proceedings of the Workshop on the Algorithmic Foundations of Robotics*, pages 11–26, 2004.
- [94] C. B. Trevarthen. Two mechanisms of vision in primates. *Psychologische Forschung*, 31(4):299–337, 1968.
- [95] S. Ullman. On visual detection of light sources. *Biological Cybernetics*, 21(4):205–212, 1976.
- [96] I. Ulrich and I. Nourbakhsh. Appearance-based place recognition for topological localization. In *Proceedings of the IEEE International Conference on Robotics and Automation (ICRA)*, pages 1023–1029, Apr. 2000.
- [97] L. Van Gool, T. Moons, D. Ungureanu, and E. Pauwels. Symmetry from shape and shape from symmetry. *International Journal Of Robotics Research*, 14(5):407–424, October 1995.
- [98] J. Wang, S. Chao, and A. Agogino. Sensor noise model development of a longitudinal positioning system for avcs. In *Proceedings of the 1999 American Control Conference*, 1999, volume 6, pages 3760–3764, 1999.
- [99] G. Welch and G. Bishop, 1995. An Introduction to the Kalman Filter, http://www.cs.unc.edu/~welch/kalman/.
- [100] J. S. Werner and L. M. Chalupa. *The visual neurosciences*. The MIT Press, 2004.
- [101] H. Weyl. Symmetry. Princeton Univ. Press, Princeton, NJ, 1952.

- [102] R. M. Wilkie, J. P. Wann, and R. S. Allison. Active gaze, visual look-ahead, and locomotor control. *Journal Of Experimental Psychology. Human Perception* and Performance, 34(5):1150–64, Oct. 2008.
- [103] A. Witkin. Scale space filtering. In Proceedings of the International Joint Conference on Artificial Intelligence, 1983.
- [104] H. Zabrodsky, S. Peleg, and D. Avnir. Symmetry as a continuous feature. Pattern Analysis and Machine Intelligence, IEEE Transactions on, 17(12):1154 –1166, Dec. 1995.